



# Unraveling kinetics and mechanism of electrocatalytic hydrodechlorination of chlorinated PPCPs by nickel-cobalt metal organic framework supported palladium composite electrode

Junjing Li<sup>a,\*</sup>, Yu Wang<sup>a</sup>, Bin Zhao<sup>a</sup>, Jing Ding<sup>b</sup>, Jun Zhang<sup>b</sup>, Menghua Yin<sup>a</sup>, Zhaohui Zhang<sup>a</sup>, Shumin Ma<sup>a</sup>, Yaqian Liu<sup>a</sup>, Zilin Tan<sup>a</sup>, Hongwei Zhang<sup>a</sup>, Liang Wang<sup>a,\*</sup>, Dionysios D. Dionysiou<sup>c</sup>

<sup>a</sup> School of Environmental Science and Engineering, Tiangong University, State Key Laboratory of Separation Membranes and Membrane Processes, Binshui West Road 399, Xiqing District, Tianjin 300387, PR China

<sup>b</sup> School of Environment, Harbin Institute of Technology, State Key Laboratory of Urban Water Resource and Environment, Huanghe Road 73, Nangang District, Harbin 150090, PR China

<sup>c</sup> Environmental Engineering and Science Program, Department of Chemical and Environmental Engineering (ChEE), University of Cincinnati, Cincinnati, OH 45221-0012, USA

## ARTICLE INFO

### Keywords:

Electrocatalytic hydrodechlorination  
Atomic H<sup>\*</sup>  
Chlorinated PPCPs  
NiCo-MOF support structure  
Removal mechanism

## ABSTRACT

In this work, a nickel-cobalt bimetallic organic framework (NiCo-MOF) was introduced as an intermediate layer to synthesize a Pd/NiCo-MOF/Nickel foam composite electrode, which was applied for electrocatalytic hydrodechlorination (ECH) of chlorinated pharmaceuticals and personal care products (PPCPs). The introduction of the NiCo-MOF structure dramatically improved the catalytic activity compared with the common Pd/Nickel foam electrode. Combined with transmission electron microscope and X-ray absorption fine structure analysis, catalyst on Pd/NiCo-MOF/Nickel foam surface had smaller particle size. The removal of the Pd/NiCo-MOF/Nickel foam electrode for chloramphenicol (CAP) reached more than 95 % at 40 min, while the removal of the Pd/Nickel foam electrode was only approximately 55 %. In this study, the active atomic hydrogen (H<sup>\*</sup>) adsorbed on the Pd and NiCo-MOF structures is the critical active species to remove chlorinated PPCPs by Pd/NiCo-MOF/Nickel foam electrode. Density functional theory (DFT) was used to calculate and investigate the adsorption strength of the composite electrode structure for CAP, the product and H<sup>\*</sup>. This work provided a new method to achieve higher catalytic performance and reactivity operability and longevity of catalytic materials through the synergism of a NiCo-MOF interlayer with Pd particles.

## 1. Introduction

In recent years, pharmaceuticals and personal care products (PPCPs) have attracted significant attention because of their rapid development [1]. PPCPs, as a class of commonly used therapeutic drugs for humans and animals, have reached a high concentration range in certain water bodies. For example, chloramphenicol has reached a high concentration (mg L<sup>-1</sup>) in pharmaceutical wastewater [2–4]. These compounds may have an influence on human and environmental health. The United States Environmental Protection Agency (US EPA) considers PPCPs to be contaminants of emerging concern [5]. Because of their poor biodegradability, some of these PPCP compounds as well as some of their

potentially harmful removal (transformation) products are still present in effluent water after treatment, raising concerns for environmental systems and human health [6,7]. Biodegradation [8,9], chemical reduction [10], advanced oxidation [11,12], and other treatment methods for PPCPs have been reported in the literature. It is imperative to develop a green and economical wastewater treatment method because of the limitations of biodegradation in practical applications [13] and the toxic byproducts produced in chemical reduction and advanced oxidation processes [14,15]. To overcome these shortcomings, scholars have focused on the development of a heterogeneous catalyst for the Fenton oxidation in recent years. Iron-containing catalysts such as zero valent iron (Fe<sup>0</sup>) and goethite (α-FeOOH), have been used to

\* Corresponding authors.

E-mail addresses: [junjingli85@163.com](mailto:junjingli85@163.com) (J. Li), [mashi7822@163.com](mailto:mashi7822@163.com) (L. Wang).

<https://doi.org/10.1016/j.apcatb.2023.122754>

Received 20 December 2022; Received in revised form 27 March 2023; Accepted 9 April 2023

Available online 11 April 2023

0926-3373/© 2023 Elsevier B.V. All rights reserved.

remove chlorophenols by heterogeneous Fenton oxidation [16]. However, the catalysts in aqueous solution is difficult to recover.

The electrocatalytic hydrodechlorination (ECH) process has been widely used for its high removal performance, mild reaction conditions, and lower secondary pollution [17–20]. In the process of ECH, the cathode is modified with a precious metal catalyst, and the active atom  $H^*$  can be adsorbed on the catalyst surface to improve the activity of the catalyst [21,22]. Palladium (Pd) is most widely used because of its higher adsorption and storage capacity for  $H^*$  compared to other precious metals (such as silver [23] and gold). Jiang et al. [24] and Liu et al. [25] found that the extent of removal of chlorinated organic pollutants reached more than 90 % by modifying the cathode with palladium nanoparticles (Pd NPs). However, electrodes made by loading Pd on the substrate alone have the problems of large particle size, easy aggregation, and low utilization efficiency of Pd particles [26]. To control the dispersion and particles size of Pd NPs, several studies have focused on a variety of carrier materials to support Pd catalysts [27]. Many previous studies have used alumina [28], silica [29,30], activated carbon fibers [31], and other porous materials as carriers. However, electrodes prepared by using these materials as carriers often have low dechlorination efficiency, and Pd NPs detach easily, which is a major disadvantage of the practical application and reuse of electrodes.

Metal-organic frameworks (MOFs) are porous materials with three-dimensional frame structures composed of metal ions or clusters and organic complexes [32]. MOF materials have high porosity and rapid charge transfer capability [33]. The use of MOFs as a support to prepare metal nanoparticle/metal-organic framework composites can significantly reduce the aggregation of nanoparticles and can help control the nanoparticles size [34,35]. In addition, MOFs can act synergistically with metal nanoparticles by providing additional active sites so that such complexes can exhibit properties different from the properties of their constituents [36,37]. Metal nanoparticle/metal-organic scaffold complexes have been widely used in adsorption [38] and storage [39], sensing [40,41], catalysis [42] and other fields. Chen et al. [43] proposed a high-performance catalyst based on a dual organic framework for water electrolysis to produce sustainable hydrogen fuel. Li et al. [44] prepared Mn(II)-based MOF materials as catalysts to achieve oxygen reduction reaction. . Owing to the synergism of Ni and Co, NiCo-based MOF electrode materials not only have excellent specific capacitance and conductivity but also have excellent electrocatalytic performance [45–48]. Therefore, it is expected in this study that NiCo-MOF and Pd particles can exhibit synergistic effects in increasing the quantity and storage of  $H^*$  and therefore improve the performance of ECH.

In this study, a NiCo-MOF/Nickel foam electrode modified with Pd NPs was prepared using NiCo-MOF as the intermediate layer to control the aggregation of Pd particles and increase the number of active surface sites to obtain a higher catalytic activity. The local structure and chemical properties around Pd species were monitored by X-ray absorption fine structure (XAFS). Chloramphenicol (CAP), sodium diclofenac (DCF), and triclosan (TCS) were selected as typical chlorinated PPCPs. The electrocatalytic dechlorination of chlorinated PPCPs was studied with a Pd/NiCo-MOF/Nickel foam electrode, which was used as cathode. In addition, the adsorption strength of the electrode for CAP, products and  $H^*$  was calculated and analyzed by density functional theory (DFT). The catalytic mechanism and kinetics of Pd/NiCo-MOF/Nickel foam electrode for chlorinated PPCPs were investigated, highlighting the role of the MOF intermediate layer in the ECH process. Finally, the operability and longevity of the electrode were proven by repeated ECH processes and various characterization methods.

## 2. Experimental section

### 2.1. Reagents and materials

Chloramphenicol (CAP), diclofenac sodium (DCF), triclosan (TCS), 5,5'-dimethyl-1-pyrroline *N*-oxide (DMPO) and palladium chloride

(PdCl<sub>2</sub>) were bought from Shanghai Aladdin Biochemical Technology Co., Ltd., China. Terephthalic acid (C<sub>8</sub>H<sub>6</sub>O<sub>4</sub>) and *N,N*-dimethylformamide (DMF) were ordered from Tianjin Jiangtian Chemical Technology Co., Ltd., China. Co(NO<sub>3</sub>)<sub>2</sub>•6H<sub>2</sub>O was ordered from Tianjin Kemio Chemical Reagent Co., Ltd., China. Ni(NO<sub>3</sub>)<sub>2</sub>•6H<sub>2</sub>O and acetone (99.75 % purity) were purchased from Tianjin Fengchuan Chemical Reagent Technology Co., Ltd., China. A proton exchange membrane (Nafion-117) was obtained from DuPont. Nickel foam (surface density = 420 g m<sup>-2</sup>, hole number = 110 PPI) was obtained from Heze Tianyu Science and Technology Development Co., Ltd., China. Methanol used was of high purity chromatography grade.

### 2.2. Preparation of electrodes

#### 2.2.1. Preparation of NiCo-MOF on nickel foam

In this process, NiCo-MOF was prepared on nickel foam by a one-step hydrothermal method. The nickel foam was pretreated by ultrasonic treatment of acetone, a certain amount of ultrapure water and 0.5 mol L<sup>-1</sup> sulfuric acid as the substrate for preparing NiCo-MOF. First, 0.5 mmol C<sub>8</sub>H<sub>6</sub>O<sub>4</sub>, 0.2 mmol Co(NO<sub>3</sub>)<sub>2</sub>•6H<sub>2</sub>O, 0.3 mmol Ni(NO<sub>3</sub>)<sub>2</sub>•6H<sub>2</sub>O and 18 mL DMF were mixed and stirred at 25 °C for 15 min. Then, 2 mL of ethanol-water mixed solution in equal proportions was added and stirred to form the precursor solution. The pretreated nickel foam (2 × 2 cm<sup>2</sup>) was immersed in the precursor solution and reacted in an autoclave at 150 °C for 12 h. After the reaction, the NiCo-MOF/Nickel foam was ultrasonically washed and dried. The molar sum of Ni(NO<sub>3</sub>)<sub>2</sub>•6H<sub>2</sub>O and Co(NO<sub>3</sub>)<sub>2</sub>•6H<sub>2</sub>O was 0.5 mmol, which was recorded as NiCo-MOF<sub>0.5</sub>/Nickel foam. The molar sum of Ni(NO<sub>3</sub>)<sub>2</sub>•6H<sub>2</sub>O and Co(NO<sub>3</sub>)<sub>2</sub>•6H<sub>2</sub>O was adjusted to 0.25, 1.0 and 2.0 mmol to synthesize different contents of Ni-Co bimetallic organic frameworks. We named these NiCo-MOF/Nickel foam electrodes NiCo-MOF<sub>0.25</sub>/Nickel foam, NiCo-MOF<sub>1</sub>/Nickel foam, and NiCo-MOF<sub>2</sub>/Nickel foam.

#### 2.2.2. Preparation of Pd/NiCo-MOF/Nickel foam electrode

A Pd/NiCo-MOF/Nickel foam electrode was prepared by the electrodeposition method with the NiCo-MOF/Nickel foam electrode as the cathode and a platinum plate (1 × 2 cm<sup>2</sup>) as the anode. Pd/NiCo-MOF/Nickel foam electrodes were prepared by electrodeposition of 0.25 mmol L<sup>-1</sup> PdCl<sub>2</sub> and 0.75 mmol L<sup>-1</sup> NaCl mixed solution for 2 h at 40 °C water bath temperature and 7 mA constant current. Similarly, Pd/Nickel foam electrode was prepared under the same electrodeposition conditions with nickel foam (2 × 2 cm<sup>2</sup>) as cathode and platinum plate (1 × 2 cm<sup>2</sup>) as anode. The preparation process for the Pd/NiCo-MOF/Nickel foam electrode is illustrated in Scheme S1.

### 2.3. Electrocatalytic hydrodechlorination tests

The ECH of CAP was conducted in an H-type electrochemical cell with the Pd/NiCo-MOF/Nickel foam electrode as the working electrode. The anolyte and catholyte were 50 mL 0.05 mol L<sup>-1</sup> Na<sub>2</sub>SO<sub>4</sub> solution and 50 mL CAP solution mixed with 0.05 mol L<sup>-1</sup> Na<sub>2</sub>SO<sub>4</sub>, respectively. The initial concentration of CAP, DCF and TCS are 35, 20 and 5 mg L<sup>-1</sup>, respectively. Detailed experimental conditions were in the supporting information (Text S1).

### 2.4. Material characterization and test methods

Scanning electron microscopy (SEM, Quanta FEG 250, USA) and energy dispersive X-ray spectroscopy (EDS) were used to characterize the morphology of the electrode materials. The lattice size of the electrode was investigated by transmission electron microscopy (TEM, JEM-2100F, Japan). The crystal structure of the electrode was analyzed by X-ray diffractometry (XRD). The instrument model was DMAX-2500/PC (Cu K<sub>α</sub>, 40 kV, 150 mA, 8° min<sup>-1</sup> 3–100°). X-ray photoelectron spectroscopy (XPS, Thermo Scientific K-Alpha, USA) was used to investigate the valence states of each component on the electrode surface. The

recording and analysis details of the Pd K-edge XAFS spectra are in the [supporting information](#) (Text S2). Electrochemical performance analysis of the electrodes was performed at the CHI660E electrochemical workstation (Shanghai Chenhua, China), including cyclic voltammetry (CV) and electrochemical impedance spectroscopy (EIS). The Ag/AgCl electrode ( $3.0 \text{ mol L}^{-1}$  KCl) is the reference electrode, and the platinum electrode is the counter electrode. The charge transfer resistance of the electrode was fitted by ZView2. Detailed experimental conditions were in the [supporting information](#) (Text S3). The electron spin resonance (ESR) signals of  $\text{H}^*$  radicals trapped by DMPO were detected by a Brooke A300 spectrometer. The concentrations of CAP, DCF, and TCS were tested by high-performance liquid chromatography (HPLC) using a Shimadzu LC-20AT model. Detailed experimental conditions for HPLC were in the [supporting information](#) (Text S4). The products of CAP in ECH process were studied by liquid chromatography-mass spectrometry (LC-MS, thermo scientific Ultimate 3000 UPLC/Q Exactive, USA). In addition, the concentration of chloride ions in catholyte was determined by ion chromatograph (IC, Dionex ICS-1000, USA). The leaching of Pd particles in ECH was determined by inductively coupled plasma emission spectrometer (ICP-OES, PerkinElmer Avio 200, USA). The electrochemical active surface area (ECSA), reaction kinetics and current efficiency (CE) calculation was introduced in [Text S5](#).

## 2.5. DFT calculations

DFT calculations were performed on the Vienna ab initio simulation package (VASP) 5.4.4 [49]. The geometric optimization was carried out until the Hellmann–Feynman force on each atom was smaller than  $0.04 \text{ eV \AA}^{-1}$ . The energy criterion was set to  $10^{-6} \text{ eV}$  in the iterative solution of the Kohn–Sham equation. A  $1 \times 2 \times 1$  supercell of MOF was constructed to study atomic  $\text{H}^*$  adsorption. The (010) slab of MOF was cleaved, and a Pd cluster with four atoms was placed on top of the (010) surface. The vacuum above the (010) surface was set to  $18 \text{ \AA}$ . The adsorption of CAP, product and  $\text{H}^*$  on the slab model was investigated. The adsorption energy ( $E_{\text{ads}}$ ) is defined as:

$$E_{\text{ads}} = E_{\text{tot}} - E_{\text{adsorbate}} - E_{\text{adsorbent}} \quad (1)$$

where  $E_{\text{tot}}$  is the total DFT energy of the adsorbed structure,  $E_{\text{adsorbate}}$  is the DFT energy of the adsorbate and  $E_{\text{adsorbent}}$  is the DFT energy of the adsorbent.

The  $d$ -band center ( $\epsilon_d$ ) and  $d$ -partial density of states ( $d$ -PDOS) of Pd are studied and discussed by the constructed Pd/NiCo-MOF structure model. The electronic properties of the Pd/NiCo-MOF structure are closely related to its structural stability [14].

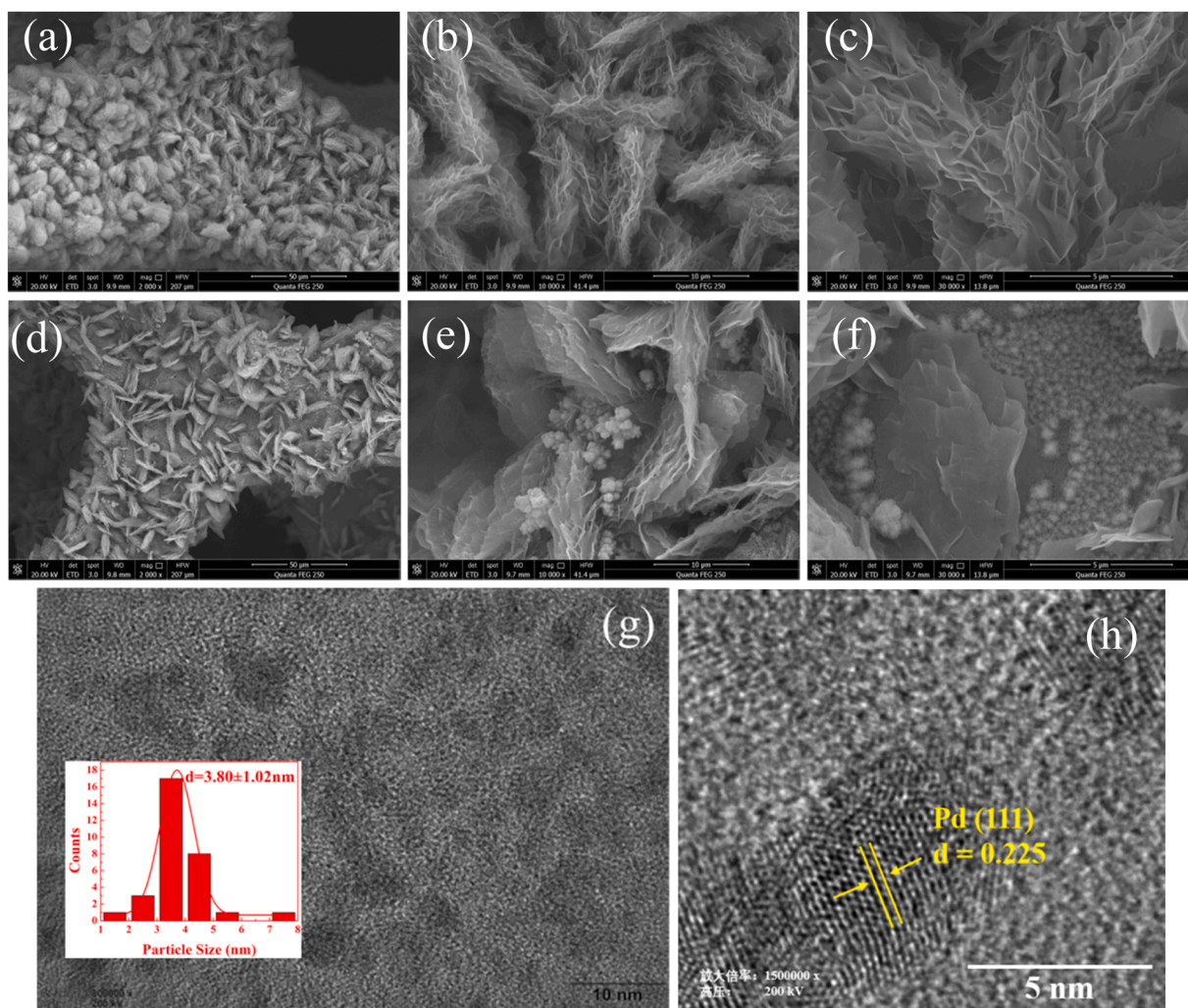


**Fig. 1.** SEM images of NiCo-MOF/Nickel foam (a (2000 $\times$ ), b (10,000 $\times$ ), c (30,000 $\times$ )); Pd/NiCo-MOF/Nickel foam (d (2000 $\times$ ), e (10,000 $\times$ ), f (30,000 $\times$ )); TEM (g) and HRTEM (h) images of Pd/NiCo-MOF/Nickel foam (inset of Fig. 1g is the histogram of statistical analysis of Pd particle size).



### 3. Results and discussion

#### 3.1. Morphological and structural characteristics

The surface morphology and structural characteristics of the Nickel foam, Pd/Nickel foam, NiCo-MOF/Nickel foam and Pd/NiCo-MOF/Nickel foam electrode were analyzed by scanning electron microscopy (SEM). The bare nickel foam (Fig. S1a) showed numerous three-dimensional pore structures and had a sufficiently smooth surface. However, dense spherical clusters of irregularly shaped Pd particles were found on the Pd/Nickel foam electrode after electrodeposition (Fig. S1b). As shown in Fig. 1a-c, NiCo-MOF nanoclusters were composed of many petal-like nanosheets, which neatly and compactly covered the surface of the nickel foam. These nanoclusters interconnected with each other on the nickel foam to form a spatial bridging structure, which was beneficial to afford surface active sites to improve the efficiency of electron transfer. Furthermore, the catalytic performance of the electrode was greatly affected by the uniform loading of Pd NPs on the electrode clusters with rough surfaces and concave and convex structures (Fig. 1d-f). In Fig. 1e and f, some of the particles we observe are palladium metal particles. The Pd/NiCo-MOF/Nickel foam electrode was characterized by EDS and element mapping to study the content and distribution of elements on the Pd/NiCo-MOF/Nickel foam composite electrode (Fig. S2 and S3). According to the SEM image of the composite electrode and the mapping of Ni, Co and Pd elements, the nickel foam was directly covered by the NiCo-MOF intermediate layer, most Pd particles were directly loaded on the MOF layer, and a few were attached to the exposed nickel foam.

The particle size and lattice fringe of the catalyzed metal on the top of the Pd/NiCo-MOF/Ni electrode were analyzed via TEM. Statistical analysis shows that the average diameter of Pd was approximately 3.80 nm (Fig. 1g), which was smaller than the average particle size of the TiN-Pd electrode, C-Pd electrode (5.2 nm) [50] and Pd@Ni-foam

electrode (8.9 nm) [51]. The experimental results indicated that the dispersion of Pd catalyst nanoparticles were improved to a certain extent because of the NiCo-MOF interlayer. In addition, due to the three-dimensional spatial network structure of NiCo-MOF nanoclusters in the Pd/NiCo-MOF/Ni electrode, the smaller as well as more dispersed Pd NPs can increase the surface active sites to increase area in contact with pollutants, which is beneficial to improve electrocatalytic performance. The High-Resolution TEM (HRTEM) image of Fig. 1h indicated that the  $\sim 0.225$  nm lattice spacing was assigned to the (111) atomic plane with face-centered cubic (fcc) Pd.

The crystal structure of the electrode was determined by X-ray diffraction (XRD). The XRD patterns (Fig. 2a and Fig. S4) of the Pd/Nickel foam, NiCo-MOF/Nickel foam, and Pd/NiCo-MOF/Nickel foam electrodes at  $44.24^\circ$ ,  $51.66^\circ$  and  $76.02^\circ$  ( $2\theta$ ) corresponded to the (111), (200) and (222) planes of Ni, respectively. The electrodes were all based on nickel foam, and the elemental content of Ni was much higher than the content of NiCo-MOF and Pd, so the diffraction peak intensities of NiCo-MOF and Pd were much weaker than the diffraction peak intensity of Ni. However, from the partial XRD patterns of the NiCo-MOF/Nickel foam and Pd/NiCo-MOF/Nickel foam electrode (Fig. S4a), the diffraction peaks of NiCo-MOF at  $8.8^\circ$ ,  $14.0^\circ$ ,  $15.6^\circ$  and  $17.7^\circ$  ( $2\theta$ ) pointed to the (200), (001), (201) and  $(\bar{2}01)$  characteristic surfaces of  $\text{Ni}_2(\text{OH})_2(\text{C}_8\text{H}_4\text{O}_4)$ , respectively [52]. In this structure, both the Co and Ni atoms were octahedrally coordinated by six O atoms (Fig. 10). These octahedra were further connected with each other in the (200) crystallographic plane to form two-dimensional metal layers. Moreover, since the largest exposed surface of NiCo-MOF was the (200) plane where the metal atoms were tightly packed, the structure was obvious at a peak of  $8.8^\circ$  ( $2\theta$ ). The sharp peak at  $39.78^\circ$  ( $2\theta$ ) corresponded to the (111) crystal plane of palladium (Fig. 2a and Fig. S4b), which was consistent with the HRTEM analysis results.

The valence analysis of the Pd/NiCo-MOF/Nickel foam electrode was analyzed by X-ray photoelectron spectroscopy (XPS), as depicted in

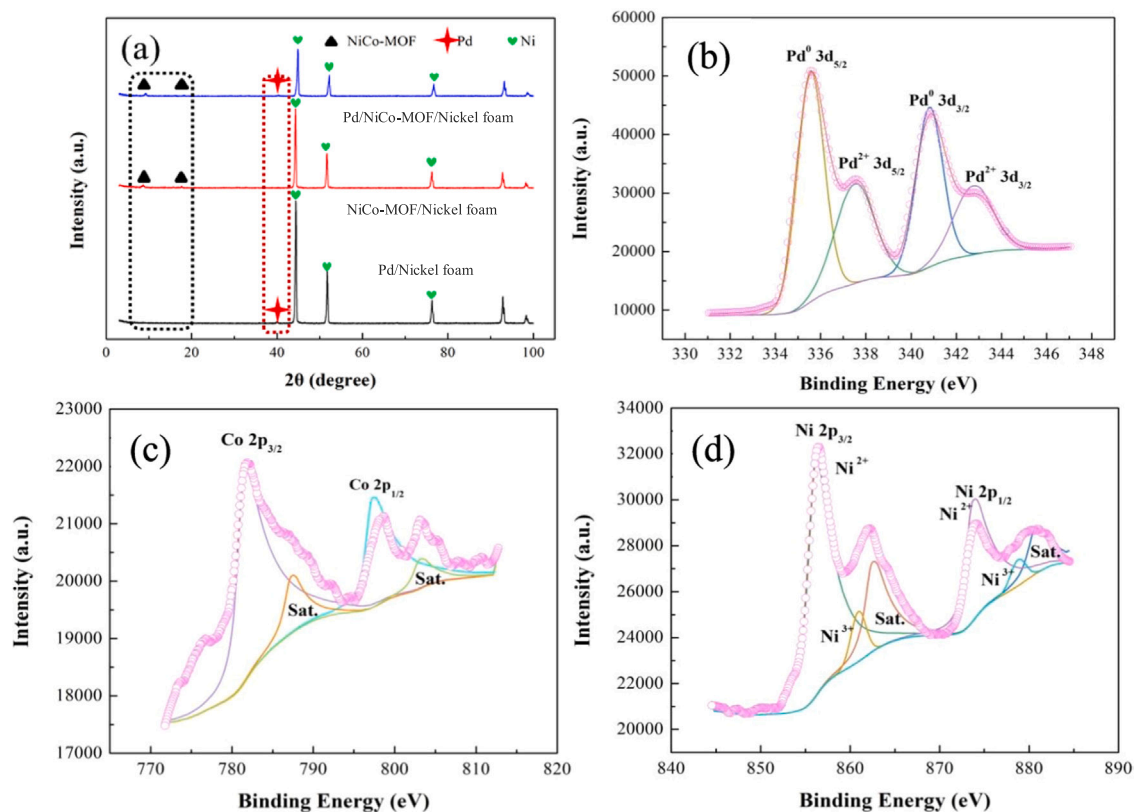


**Fig. 2.** XRD patterns of Pd/Nickel foam, NiCo-MOF/Nickel foam, and Pd/NiCo-MOF/Nickel foam electrode (a); XPS spectra of Pd/NiCo-MOF/Nickel foam electrode: Pd 3d (b); Co 2p (c); Ni 2p (d).

Fig. 2b-d, Fig. S5 and S6. It was shown that the components of the Pd/NiCo-MOF/Nickel foam electrode consisted of O, C, Pd, Ni, Co, etc., consistent with the EDS (Fig. S2) results. The C 1s XPS spectrum (Fig. S6a) showed that the peak at 284.7 eV binding energy corresponded to the carbon on the benzene ring of terephthalic acid, and the peak at 288.5 eV binding energy corresponded to the carboxylic acid (O-C=O) group on terephthalic acid [53]. The XPS spectrum of Co 2p was displayed in Fig. 2c. The peaks at 781.4 eV and 797.4 eV belong to the characteristic peaks of Co 2p<sub>3/2</sub> and Co 2p<sub>1/2</sub> [54,55], while the binding energies at 785.9 eV and 802.9 eV correspond to their satellite peaks, respectively. The XPS spectra of Ni 2p (Fig. 2d) showed that the two principal peaks of Ni 2p<sub>3/2</sub> and Ni 2p<sub>1/2</sub> were at 856.0 eV and 873.6 eV, respectively, while the positions of 861.8 eV and 880.2 eV belong to the Ni 2p satellite peaks [56]. Meanwhile, there were a few Ni<sup>3+</sup> peaks in the Ni 2p spectrum. The Pd 3d XPS spectrum of the Pd/NiCo-MOF/Nickel foam electrode is presented in Fig. 2b, in which the Pd 3d core layer is divided into 3d<sub>5/2</sub> (~335.3 eV) and 3d<sub>3/2</sub> (~340.5 eV) states [50]. However, the signal peak of the second pair of Pd 3d appeared at 337.5 eV and 343.0 eV, which was caused by the presence of Pd atoms (Pd<sup>2+</sup>) with a higher charge density in the electrode. Pd has a strong ability to adsorb and store H\*, but zero-valent palladium plays an important role in ECH process [21,50]. Further combined with the quantitative analysis of various components of Pd 3d in Table 1, it can be seen that zero-valent palladium was the main component of Pd in the Pd/NiCo-MOF/Nickel foam electrode, accounting for 65.4 %, which indicates the excellent electrocatalytic activity of the electrode.

To further reveal the local structure and chemical coordination environment of Pd/Nickel foam and Pd/NiCo-MOF/Nickel foam, XAFS spectra were further recorded [57,58]. X-ray absorption near edge structure (XANES) spectra of Pd K-edge showed that the absorption edges of Pd/Nickel foam and Pd/NiCo-MOF/Nickel foam were between 0 and 2 valence states (Fig. 3a). It was proved that Pd particles in both electrodes had partial oxidation, which was consistent with XPS results. The K space data of Extended X-ray absorption fine structure spectrum (EXAFS) spectra indicated that the high k-region oscillation signal caused by metal interaction and the low k-region signal caused by light elements (Table 2), indicating the existence of Pd-O and Pd-Pd (Fig. 3b, Fig. S7). By Fourier transformation of EXAFS data into R space, the main peak corresponding to Pd-foil was found at 2.74 Å. Therefore, the coordination peak of Pd-Pd is dominant (Fig. 3c, Fig. S8). Secondly, the intensity of characteristic peak in Pd/NiCo-MOF/Nickel foam was lower compared with Pd/Nickel foam, which proved that the particle size of Pd in the latter was smaller [50,59], which was consistent with TEM analysis. To further distinguish the coordination environment of Pd, we

**Table 1**

Valence composition and quantitative analysis of Pd 3d on Pd/NiCo-MOF/Nickel foam electrode after different cycles.

Electrode	Components	Pos. (eV)	Area Ratio (%)
Pd/NiCo-MOF/Nickel foam fresh	Pd <sup>0</sup> 3d <sub>5/2</sub>	335.30	38.65
	Pd <sup>0</sup> 3d <sub>3/2</sub>	340.50	26.75
	Pd <sup>2+</sup> 3d <sub>5/2</sub>	337.50	20.45
	Pd <sup>2+</sup> 3d <sub>3/2</sub>	343.00	14.55
Pd/NiCo-MOF/Nickel foam after 5 cycles	Pd <sup>0</sup> 3d <sub>5/2</sub>	335.30	36.76
	Pd <sup>0</sup> 3d <sub>3/2</sub>	340.50	25.37
	Pd <sup>2+</sup> 3d <sub>5/2</sub>	337.50	22.43
	Pd <sup>2+</sup> 3d <sub>3/2</sub>	343.00	15.44
Pd/NiCo-MOF/Nickel foam after 15 cycles	Pd <sup>0</sup> 3d <sub>5/2</sub>	335.30	30.49
	Pd <sup>0</sup> 3d <sub>3/2</sub>	340.50	21.04
	Pd <sup>2+</sup> 3d <sub>5/2</sub>	337.50	28.65
	Pd <sup>2+</sup> 3d <sub>3/2</sub>	343.00	19.82

analyzed the wavelet transform spectrum (Fig. 3d). Obviously, Pd-Pd was the major coordination environment of Pd/NiCo-MOF/Nickel foam, while Pd in Pd/Nickel foam was more oxidized (Fig. S9).

### 3.2. Electrochemical properties

The evolution of H\* on Pd/NiCo-MOF/Nickel foam electrode was identified by CV. As the main reducing agent in the ECH process, H\* is usually generated through the reduction of hydronium ions (H<sub>3</sub>O<sup>+</sup>) and the splitting of water molecules. The formed H\*, which is adsorbed on the top of the Pd crystal and MOF molecule, can then attack and break the C-Cl bond [20,56]. The CV curves of the Pd/NiCo-MOF/Nickel foam electrode and Pd/Nickel foam electrode are shown in Fig. S10. The presence of NiCo-MOF was proven to accelerate the splitting of H-OH, produced more H\* and improved the ECH. To better study the generation and influence of H\* on the Pd/NiCo-MOF/Nickel foam electrode, the CV diagrams in sodium sulfate solution were studied in the range of -0.95 V to -1.20 V. Fig. 4a shows that oxidation peaks were found in the interval of electrode potentials of -0.70 ~ -0.40 V and -0.20 ~ -0.10 V, respectively. On the basis of the literature [60], both oxidation peaks may be connected with the oxidation of H<sub>2</sub> at -0.70 to -0.40 V and the desorption of H\* adsorbed on the polycrystalline Pd surface at -0.20 ~ -0.10 V. The CV results show that the areas of both oxidation peaks would increase due to the increase in initial potential within specified bounds. To further explore origin of the Ni XPS spectrum. The Ni XPS spectrum of NiCo-MOF was tested. As shown in the Fig. S27, the Ni XPS spectrum of NiCo-MOF was almost same as Pd/NiCo-MOF/Nickel foam (Fig. 2d) and they had equivalent Ni species. Thus, it can be inferred that Ni species of Pd/NiCo-MOF/Nickel foam result from NiCo-MOF. At the same time, the experimental results (Fig. S30) showed that Pd was the main site that generated atomic H\*.

In EIS, the charge transfer resistance is represented by the arc radius on the Nyquist diagram [14,61]. Rapid electron transferability can promote the removal of pollutants during electrocatalysis [50]. Nyquist diagrams of the Pd/NiCo-MOF/Nickel foam, NiCo-MOF/Nickel foam and Pd/Nickel foam electrodes are shown in Fig. 4b. The equivalent circuit for EIS fitting was R (RC) W. The high-frequency semicircular region is associated with charge transfer capability, and its diameter indicates the resistance (R<sub>CT</sub>) value of the electrode [62]. According to the Nyquist plots (Fig. 4b, inset was the equivalent circuit), the Pd/NiCo-MOF/Nickel foam electrode had the smallest diameter. By ZView2 fitting analysis, the charge transfer resistance values of the Pd/NiCo-MOF/Nickel foam, NiCo-MOF/Nickel foam and Pd/Nickel foam electrode were 3.242 Ω, 3.679 Ω and 4.911 Ω, respectively. The EIS fitting curve and equivalent circuit data parameters of Pd/NiCo-MOF/Nickel foam, NiCo-MOF/Nickel foam and Pd/Nickel foam electrodes were shown in the Fig. S11. Compared with the Pd/Nickel foam electrode, the lower R<sub>CT</sub> value in the Pd/NiCo-MOF/Nickel foam electrode showed that the NiCo-MOF interlayer improved the electrochemical performance of the Pd/NiCo-MOF/Nickel foam electrode material to a certain extent.

According to the Equation S1 and Fig. S10, the electrochemical active surface area (ECSA, cm<sup>2</sup>) values of the Pd/NiCo-MOF/Nickel foam electrode and Pd/Nickel foam electrode were 1.933 cm<sup>2</sup> and 0.418 cm<sup>2</sup>, respectively. Compared with the traditional electrode, the composite electrode with a NiCo-MOF interlayer had a larger electrochemical active surface area and additional active sites. The synergy parameter of NiCo-MOF and Pd was 4.98 (Text S5), which was greater than 1. Therefore, NiCo-MOF interlayer had synergy with catalytic metal Pd.

### 3.3. Electrocatalytic hydrodechlorination

As shown in Fig. S12, we performed adsorption experiments on CAP with Nickel foam, Pd/Nickel foam, NiCo-MOF/Nickel foam and Pd/NiCo-MOF/Nickel foam electrode, prior to the ECH experiment. It has

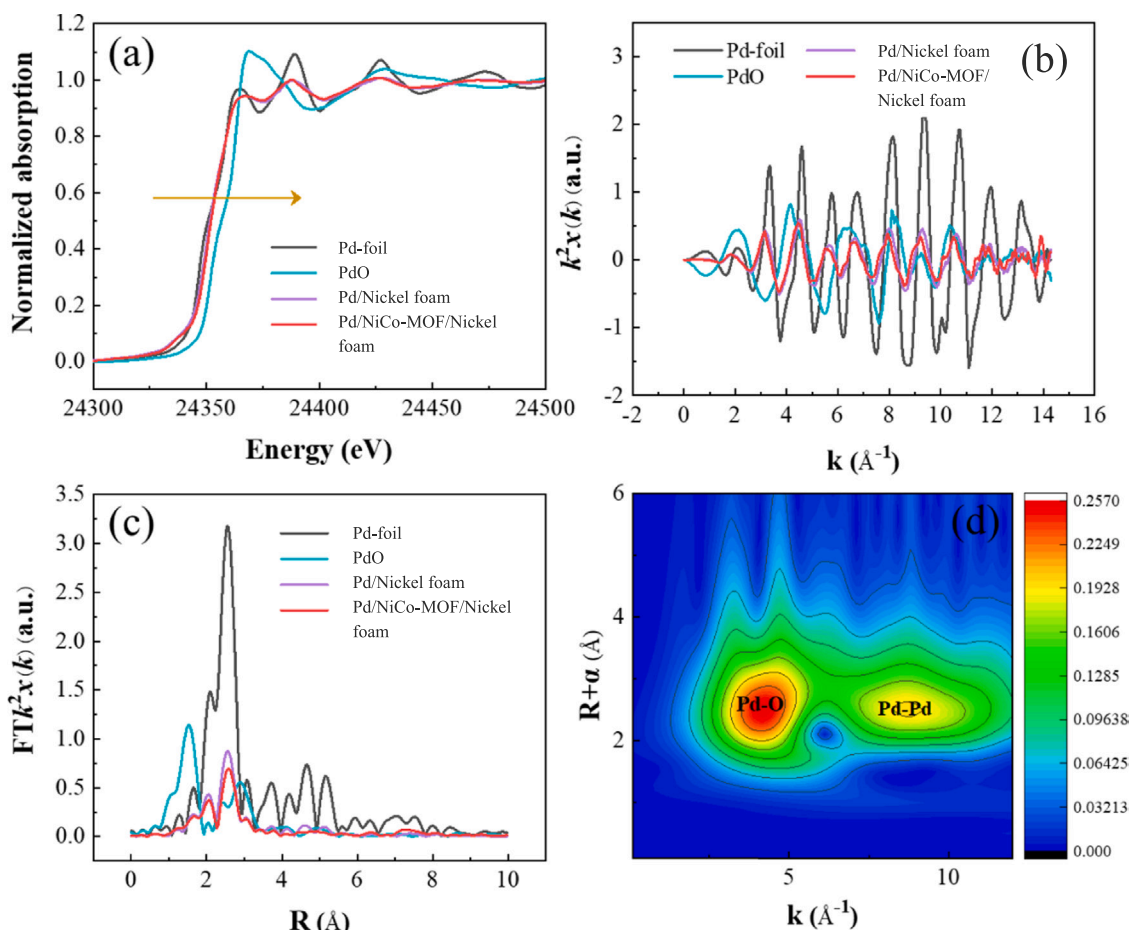


**Fig. 3.** (a) XANES spectra of Pd K-edge; EXAFS spectra of Pd K-edge in (b) K space and (c) R space. (d) Wavelet transform spectra for the  $k^2$ -weighted EXAFS signals of Pd/NiCo-MOF/Nickel foam.

**Table 2**  
EXAFS fitting parameters at the Pd K-edge for various samples.

Sample	Shell	CN	R ( $\text{\AA}$ )	$\sigma^2$ ( $\text{\AA}^2$ )	$\Delta E_0$ (eV)	R factor (%)
Pd foil	Pd-	12	2.72	0.0075	5.31	0.60
	Pd		$\pm 0.013$		$\pm 2.02$	
Pd/Nickel foam	Pd-O	4.0	2.16	0.0078	4.88	0.35
		$\pm 0.2$	$\pm 0.035$		$\pm 3.25$	
	Pd-	10.1	2.75	0.0070	5.79	
	Pd	$\pm 0.3$	$\pm 0.040$		$\pm 0.59$	
Pd/NiCo-MOF/Nickel foam	Pd-O	3.8	2.21	0.0028	3.32	0.90
		$\pm 0.1$	$\pm 0.023$		$\pm 2.96$	
	Pd-	8.5	2.77	0.0084	4.38	
	Pd	$\pm 0.2$	$\pm 0.048$		$\pm 0.67$	

CN, coordination number; R, distance between absorber and backscatter atoms;  $\sigma^2$ , Debye-Waller factor to account for both thermal and structural disorders;  $\Delta E_0$ , inner potential correction; R factor indicates the goodness of the fit.  $S_0^2$  was fixed to 0.80, according to the experimental EXAFS fit of Pd foil by fixing CN as the known crystallographic value. Fitting range:  $3.0 \leq k$  ( $\text{\AA}^{-1}$ )  $\leq 12$  and  $1.0 \leq R$  ( $\text{\AA}$ )  $\leq 3.0$  (Pd foil);  $3.0 \leq k$  ( $\text{\AA}^{-1}$ )  $\leq 12.0$  and  $1.0 \leq R$  ( $\text{\AA}$ )  $\leq 3.2$  (Sample Pd). A reasonable range of EXAFS fitting parameters:  $0.700 < S_0^2 < 1.000$ ;  $CN > 0$ ;  $\sigma^2 > 0 \text{ \AA}^2$ ;  $\Delta E_0 < 10 \text{ eV}$ ; R factor  $< 0.02$ .

been proved that Nickel foam, Pd/Nickel foam, NiCo-MOF/Nickel foam and Pd/NiCo-MOF/Nickel foam electrode had little adsorption effect on CAP. The ECH performance of the Pd/Nickel foam, NiCo-MOF/Nickel foam and Pd/NiCo-MOF/Nickel foam electrode for CAP was shown in Fig. 5a. The Pd/NiCo-MOF/Nickel foam electrode showed excellent ECH performance on CAP, which can be completely removed within

120 min, while the extent of removal of CAP by using Pd/Nickel foam and NiCo-MOF/Nickel foam were 94.71 % and 80.52 %, respectively. In addition, the reaction rate constants of the Pd/Nickel foam, NiCo-MOF/Nickel foam and Pd/NiCo-MOF/Nickel foam electrode in the electrocatalytic dechlorination process of CAP were  $k_{obs1} = 0.06784 \text{ min}^{-1} > k_{obs2} = 0.02463 \text{ min}^{-1} > k_{obs3} = 0.01279 \text{ min}^{-1}$  (Fig. 5b). The removal rates ( $-d[\text{CAP}]/dt$ ,  $\text{mg L}^{-1} \text{ min}^{-1}$ ) of the Pd/Nickel foam, NiCo-MOF/Nickel foam and Pd/NiCo-MOF/Nickel foam electrodes for CAP at different time were shown in Fig. 5c. The removal rate of the Pd/NiCo-MOF/Nickel foam electrode was significantly higher than the removal rates of the other electrodes in the first 40 min. Compared with the Pd/Nickel foam and NiCo-MOF/Nickel foam electrode, the Pd/NiCo-MOF/Nickel foam electrode had better electrocatalytic performance. The experimental results were consistent with the removal results mentioned above. The ECH efficiencies of CAP with Pd/NiCo-MOF/Nickel foam composite electrodes with different contents of NiCo-MOF were shown in Fig. 5c. The best removal efficiency of CAP was 100 % by Pd/NiCo-MOF<sub>0.5</sub>/Nickel foam, and the removal of CAP by Pd/NiCo-MOF<sub>2</sub>/Nickel foam, Pd/NiCo-MOF<sub>1</sub>/Nickel foam, and Pd/NiCo-MOF<sub>0.25</sub>/Nickel foam electrodes were 93.27 %, 97.20 %, and 99.87 %, respectively. According to CAP removal data of Pd/NiCo-MOF/Nickel foam electrode with different NiCo-MOF interlayer contents (Fig. 5c), it can be seen that appropriate increase of MOF content can accelerate the removal of CAP. However, with the increase in the content of the intermediate layer, the stacking of the MOF layer affected the binding between the MOF layer and Pd particles, which reduced the removal efficiency of pollutants. The morphologies of the electrodes with different MOF contents were different (Fig. S13). The MOF layer had a lamellar structure in Pd/NiCo-MOF<sub>0.25</sub>/Nickel foam, Pd/NiCo-MOF<sub>0.5</sub>/Nickel foam and Pd/NiCo-



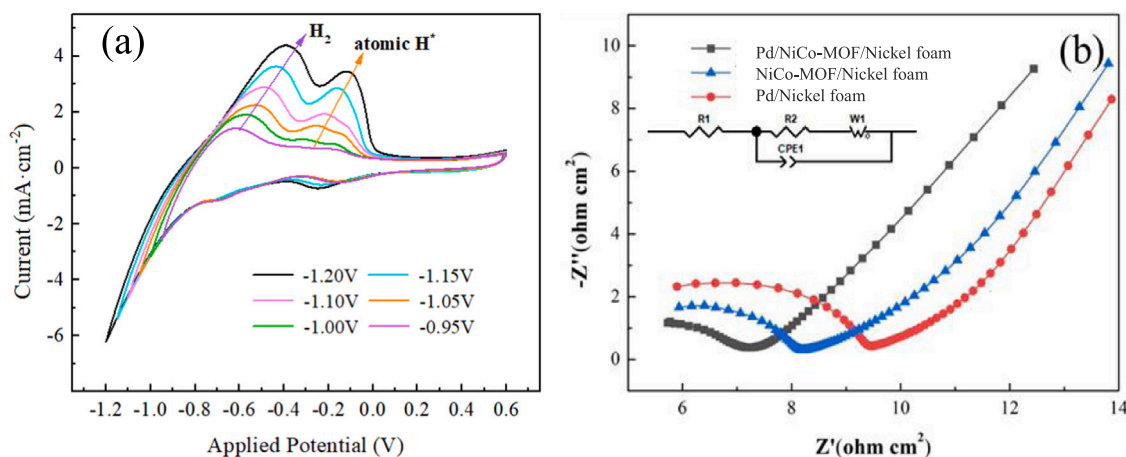


**Fig. 4.** (a) CV spectra of the Pd/NiCo-MOF/Nickel foam electrode with different starting potentials; (b) Nyquist diagram of the above three electrodes in 0.05 mol L<sup>-1</sup> Na<sub>2</sub>SO<sub>4</sub> solution. Inset is the equivalent electrical circuit used to fit the EIS data. (Conditions: electrolyte = 0.05 mol L<sup>-1</sup> Na<sub>2</sub>SO<sub>4</sub> solution, reference electrode = Ag/AgCl electrode (3.0 mol L<sup>-1</sup> KCl), pH = 6.86, initial scan polarity = positive, scan rate = 50 mV s<sup>-1</sup>, frequency range = 0.1 Hz - 1 MHz (without iR correction)).

MOF<sub>1</sub>/Nickel foam. However, the morphology of Pd/NiCo-MOF<sub>2</sub>/Nickel foam electrode was very different with others. The morphology of palladium was dendritic and its distribution was not uniform. The ECH process was the indirect reduction process mediated by the adsorbed atomic H\*, rather than the direct reduction process of chlorine-containing pollutants [63]. According to the results of CV analysis, a large number of adsorbed H\* atoms were produced during the ECH process. The removal rates of the Pd/NiCo-MOF<sub>2</sub>/Nickel foam, Pd/NiCo-MOF<sub>1</sub>/Nickel foam, Pd/NiCo-MOF<sub>0.5</sub>/Nickel foam and Pd/NiCo-MOF<sub>0.25</sub>/Nickel foam electrode for CAP at different time were shown in Fig. 5f. The experimental results indicated that compared with the other three electrodes, the Pd/NiCo-MOF<sub>0.5</sub>/Nickel foam electrode achieved the same or even better removal effect in a shorter time, which undoubtedly can save the time and economic cost of treating pollutants. The first-order dynamic model diagram illustrated in Fig. 5d further indicates that NiCo-MOF<sub>0.5</sub> can better combine with Pd NPs and has better electrocatalytic performance.

The removal results for DCF and TCS on the Pd/NiCo-MOF<sub>0.5</sub>/Nickel foam electrode were displayed in Fig. 5h. The removal of DCF and TCS by Pd/NiCo-MOF<sub>0.5</sub>/Nickel foam electrodes was shown to reach 99.81 % and 94.15 % after 120 min, respectively, further demonstrating the excellent electrocatalytic performance of the Pd/NiCo-MOF<sub>0.5</sub>/Nickel foam electrode.

Current efficiency (CE) was an important index of ECH [50]. As shown in Fig. 5g, the CE of ECH reaction at Pd/Nickel foam, NiCo-MOF/Nickel foam and Pd/NiCo-MOF/Nickel foam electrode was volcanic in the reaction period, and the CE at Pd/NiCo-MOF/Nickel foam electrode was the highest at 40 min (CE = 11.82 %). The CE of the Pd/NiCo-MOF/Nickel foam electrode was reduced after 40 min, because the concentration of CAP decreased, most electrons participated in hydrogen evolution reaction [63]. The concentration of chloride ions was determined by IC. As shown in Fig. S14, chloride ion concentration increases gradually with ECH process. Moreover, the final concentration of chloride ions was about twice that of CAP, indicating that all the chlorine atoms were finally present in the system as chloride ions.

Electric energy per order ( $E_{EO}$ ) was used to evaluate the energy consumption of the electrode during ECH. According to Equation S3, the  $E_{EO}$  of each electrode was calculated. In addition, the electric energy per order results of the electrodes was shown in Table 3. The experiment results indicated that the Pd/NiCo-MOF<sub>0.5</sub>/Nickel foam electrode had the lowest  $E_{EO}$  value. The Pd/NiCo-MOF<sub>0.5</sub>/Nickel foam electrode was proven to be competitive with other electrodes in terms of relative operating cost and treatment efficiency.

### 3.4. Stability tests

To study the operability and longevity of the composite electrode, the Pd/NiCo-MOF/Nickel foam electrode was reused to remove CAP for 15 cycles (120 min for each cycle). As shown in Fig. 6a, CAP removal efficiency of electrode was 100 % after 4 cycles, and still above 95 % after 15 cycles. In addition, we also carried out a cycle experiment on DCF with Pd/NiCo-MOF/Nickel foam electrode (Fig. 6b). After 10 cycles, the extent of removal was more than 80 %. The extent of removal after 15 cycles still reached more than 70 %. We hypothesized some reasons for the decline in the removal effect. The first reason was that the metal Pd particles detached and deactivated during the continuous dechlorination process, resulting in the reduction of active sites on the electrode surface. Further, some products did not desorb from the electrode, which inhibited contact between the pollutant and the active hydrogen (H\*). The leaching of Pd particles on Pd/NiCo-MOF/Nickel foam electrode during ECH was determined by ICP-OES. As shown in Fig. S15, Pd particles was slightly leached in the ECH process.

The Pd/NiCo-MOF/Nickel foam electrode activity was verified by XPS analysis. Fig. S6b-c showed the XPS spectra of Pd after 5 cycles and 15 cycles respectively. Table 1 showed the quantitative analysis of Pd 3d components on Pd/NiCo-MOF/Nickel foam electrode after different cycles. The data showed that the proportion of Pd<sup>0</sup> increases somewhat, while the proportion of Pd<sup>2+</sup> decreases slightly compared to that before the use of the Pd/NiCo-MOF/Nickel foam electrode, but zero-valent palladium was still the main valence state of Pd particles. Pd<sup>0</sup> was accounting for 62.13 % after 5 cycles, 51.53 % after 15 cycles. The proportion of zero-valent palladium decreased gradually, and the intensity of Pd signal peak decreased obviously after cycles. Fig. S16 showed the XPS spectra of Pd/NiCo-MOF/Nickel foam electrode after 15 cycles. Compared with the fresh Pd/NiCo-MOF/Nickel foam electrode (Fig. S5), the content of Pd decreased significantly. Fig. S17 showed XPS characterization analysis of Pd/NiCo-MOF/Nickel foam electrode after 5 cycles. The peak values of Ni<sup>2+</sup> and Co<sup>2+</sup> decreased somewhat but had little influence on the stability of the composite electrode. The surface morphology of the used electrode was characterized by SEM. The SEM figure of Pd/NiCo-MOF/Nickel foam electrode after 5 cycles showed that the NiCo-MOF nanosheets were still dense and uniform on the exposed nickel foam, the solid three-dimensional porous spatial network structure had not been destroyed, and the Pd NPs did not detach and remained firmly attached to the MOF layer (Fig. S18). EDS analysis and mapping (Fig. S19 and S20) of the Pd/NiCo-MOF/Nickel foam electrode (Fig. S18b) proved that the content of each element and its uniform distribution on the electrode surface were retained after repeated use of the electrode, confirming the excellent stability of the composite

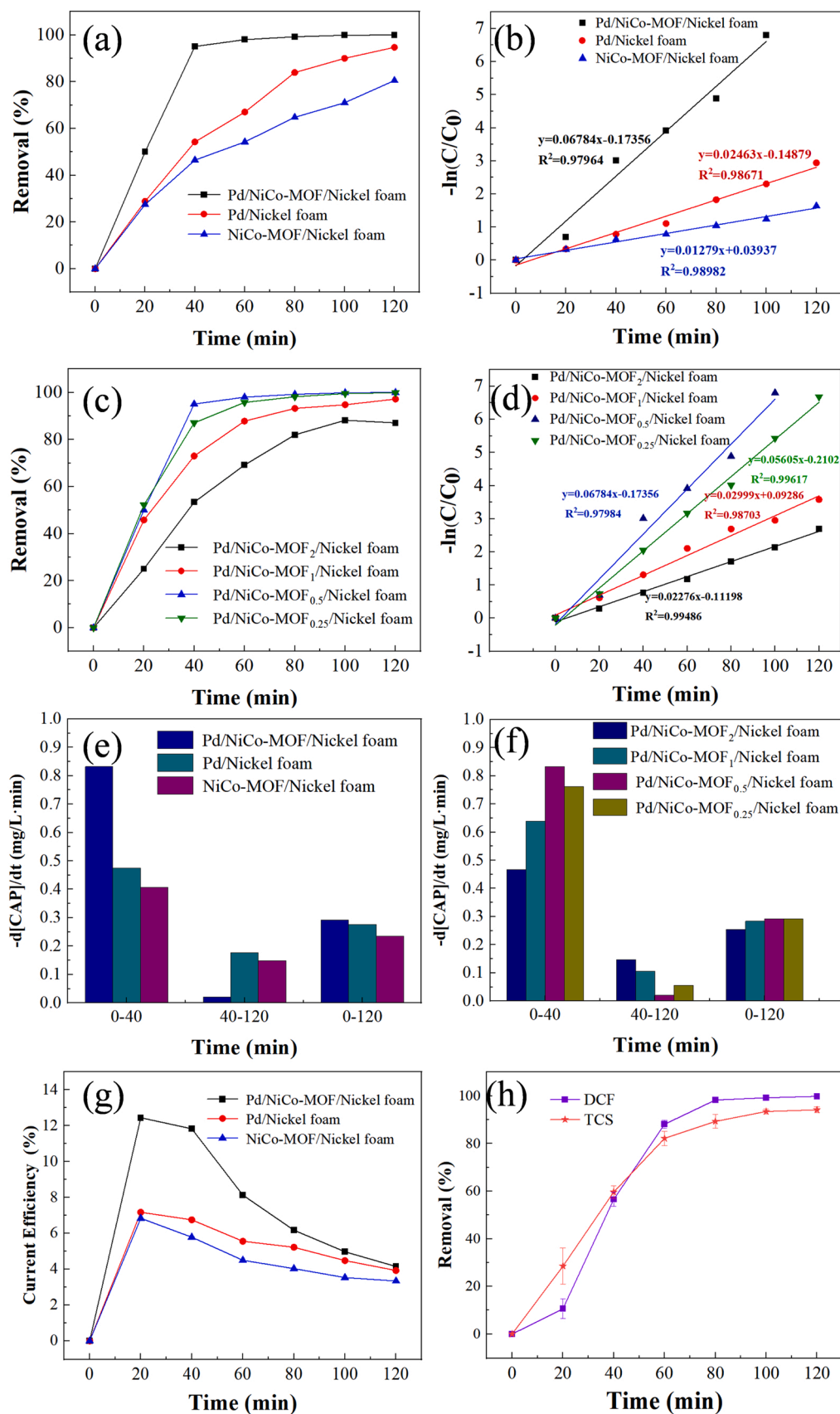


Fig. 5. (a, c) Electrochemical hydro-dechlorination of CAP; (b, d) the relevant first-order representation ( $\text{CAP}_0 = 35 \text{ mg L}^{-1}$ ,  $0.05 \text{ mol L}^{-1} \text{ Na}_2\text{SO}_4$ , applied current = 7 mA); Removal rate of CAP by (e) Pd/NiCo-MOF/Nickel foam, Pd/Nickel foam and NiCo-MOF/Nickel foam electrode; (f) Pd/NiCo-MOF<sub>2</sub>/Nickel foam, Pd/NiCo-MOF<sub>1</sub>/Nickel foam, Pd/NiCo-MOF<sub>0.5</sub>/Nickel foam and Pd/NiCo-MOF<sub>0.25</sub>/Nickel foam electrode; (g) Current efficiency of CAP; (h) Electrocatalytic performance of Pd/NiCo-MOF<sub>0.5</sub>/Nickel foam electrode for DCF and TCS.



**Table 3**

First-order kinetic constant ( $k_{obs}$ ), removal rate ( $-d[CAP]/dt$ ) and the electric energy per order ( $E_{EO}$ ) of chloramphenicol at different electrodes.

Electrode	$k_{obs}$ $\text{min}^{-1}$	$R^2$	$-d[CAP]/dt$ (0–40 min) $\text{mg L}^{-1} \text{min}^{-1}$	$E_{EO}$ ( $\text{kW h m}^{-3}$ $\text{order}^{-1}$ )
Pd/NiCo-MOF <sub>0.5</sub> /Nickel foam	0.06784	0.980	0.832	56.604
Pd/Nickel foam	0.02463	0.987	0.475	155.907
NiCo-MOF <sub>0.5</sub> /Nickel foam	0.01279	0.99	0.407	300.235
Pd/NiCo-MOF <sub>2</sub> /Nickel foam	0.02276	0.995	0.467	168.717
Pd/NiCo-MOF <sub>1</sub> /Nickel foam	0.02999	0.987	0.639	128.043
Pd/NiCo-MOF <sub>0.25</sub> /Nickel foam	0.05605	0.996	0.762	68.510

electrode. SEM images of Pd/NiCo-MOF/Nickel foam electrode after 15 cycles were displayed in Fig. S21. It can be seen from the figure that the number of Pd particles decreased and part of the NiCo-MOF frame structure was destroyed, which reduced the number of active sites on the electrode surface. However, Pd, Ni, Co and other elements were still evenly distributed on the top of electrode (Fig. S22).

### 3.5. Mechanism

The reaction products of CAP in ECH process of Pd/NiCo-MOF/Nickel foam electrode were studied through LC-MS. As shown in Fig. 7, CAP was completely reduced from the -NO<sub>2</sub> group to the -NH<sub>2</sub> group during ECH to produce the product 2 O-CAP. Subsequently, dechlorination was performed to yield two dechlorination products, Cl-2 O-CAP and 2Cl-2 O-CAP (Fig. 7b-c). The dechlorination products of DCF were determined by liquid chromatography-mass spectrometry, and the results were shown in Fig. S23. Fig. S23a shows the mass spectrum response of DCF. DCF with a 9:6:1 chlorine isotope match with an ion cluster of  $m/z$  294/296/298 in the mass spectrum. With the hydrogenation dechlorination reaction, the mono-chlorine product and the final product of DCF appeared, as shown in Fig. S23b-c, corresponding to  $m/z$  260/262 and  $m/z$  226 ion clusters, respectively. This is consistent with our previous research results [64]. TCS and its products from electrocatalytic hydrogenation dechlorination were determined by the same method. Fig. S24a shows the ion clusters of TCS with a plastic-nucleus ratio of 287/289/291/293, which is attributed to the presence of chlorine isotopes. Depending on the amount of debris in the mass spectrum, the TCS dechlorination intermediate can be identified [65]. The ion clusters shown in Fig. S24b-d are dichloro, monochloro and chlorine-free products of TCS. The chlorine-free product

2-phenoxyphenol can be further hydrogenated to obtain 6-phenoxyphenol-3-enol as shown in Fig. S24e.

Ecotoxicity analysis of CAP, DCF, TCS, and reaction products were performed using T.E.S.T software. According to the analysis results, the acute toxicity and bioaccumulation factor curves were shown in Fig. S25. Acute toxicity of CAP increased from the initial 1.61  $\text{mg L}^{-1}$  to 273.41  $\text{mg L}^{-1}$ , a 169.81-fold reduction in toxicity. The bioaccumulation factor decreased 3.28 times from  $-0.18$  to  $-0.59$ . The toxicity reduction of electrocatalytic hydrogenation dechlorination was verified. As shown in Fig. S26, after the ECH process, the lethal concentration of DCF increased by 7.75 times (DCF 0.4  $\text{mg L}^{-1}$ , P2 3.1  $\text{mg L}^{-1}$ ), and the bioaccumulation factor decreased by 0.259 times from 1.43 to 1.06. This fully confirmed that the toxicity of DCF in environmental water can be fully reduced through ECH process. In addition, T. E.S.T software was used to perform corresponding toxicity analysis for TCS, intermediates (P1, P2, P3) and end products (P4), and the results were shown in Fig. S27. The illustration represents the three isomers of P1 and P2. After ECH process, the acute toxicity concentration of TCS was increased from the original 0.12  $\text{mg L}^{-1}$  to 14.46  $\text{mg L}^{-1}$  of P4, and the toxicity was reduced by 120.50 times. The bioaccumulation factor decreased from 3.23 to 1.88, a 1.72-fold decrease.

In the ECH system, indirect reduction dechlorination by  $\text{H}^*$  is the main dechlorination pathway. To further study the indirect reduction mechanism of the Pd/NiCo-MOF/Nickel foam electrode in the ECH process, DCF dechlorination experiment was carried out with *tert*-butanol (TBA). As displayed in Fig. 8a, when the concentration of TBA increased from 0 to 2  $\text{mol L}^{-1}$ , the dechlorination efficiency of DCF by the Pd/NiCo-MOF/Nickel foam electrode changed significantly. Meanwhile, to further prove the reaction mechanism, other  $\text{H}^*$  quencher (Dimethyl sulfoxide, DMSO) was used in ECH reaction of CAP. Three concentrations of DMSO (0.1  $\text{mmol L}^{-1}$ , 0.2  $\text{mmol L}^{-1}$  and 0.5  $\text{mmol L}^{-1}$ ) were studied and the experiment results were shown in the Fig. S31. It can be seen that dechlorination efficiency decreased as DMSO concentration increased. Dechlorination efficiency was only 37 % with the presence of 0.5  $\text{mmol L}^{-1}$  DMSO, proving the reaction was an atomic  $\text{H}^*$  mediated indirect reduction mechanism. Furthermore, the formation of  $\text{H}^*$  in the ECH process of the NiCo-MOF/Nickel foam electrode and Pd/NiCo-MOF/Nickel foam electrode was verified by ESR method [14,25, 65]. Fig. 8b showed that the characteristic peaks of  $\text{H}^*$  were captured, and according to the peak intensity, the addition of the MOF interlayer on Pd/Nickel foam can further promote the generation of  $\text{H}^*$ . The ESR test confirmed that  $\text{H}^*$  was generated during the electrocatalytic reduction process. All the above results proved that dechlorination by the Pd/NiCo-MOF/Nickel foam electrode was mainly indirect hydrodechlorination mediated by  $\text{H}^*$ . The ECH process occurring on the Pd/NiCo-MOF/Nickel foam electrode can be expressed by Eqs. (2)–(5)

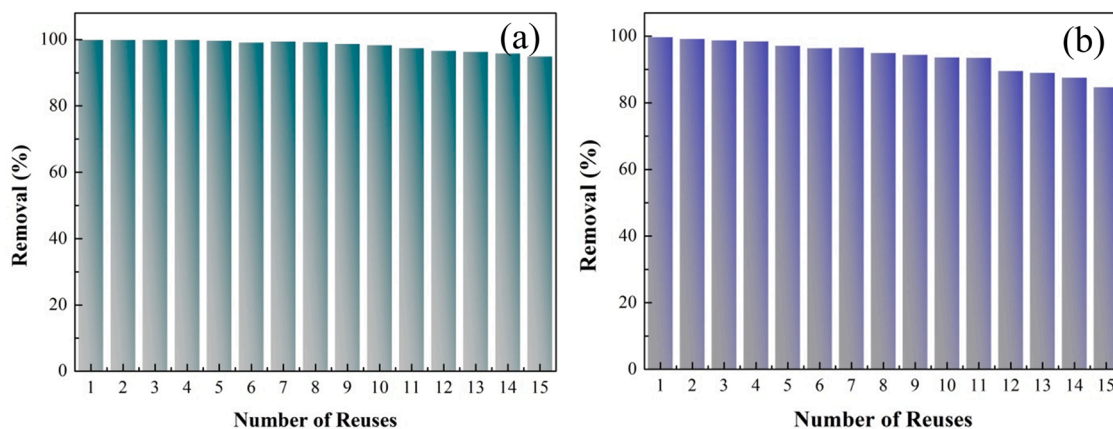


**Fig. 6.** Reusability of the Pd/NiCo-MOF/Nickel foam electrode for dechlorination of CAP (a) and DCF (b) (120 min for each cycle, a and b are under same conditions, temperature: 40 °C; current density: 1.75  $\text{mA cm}^{-2}$ ).

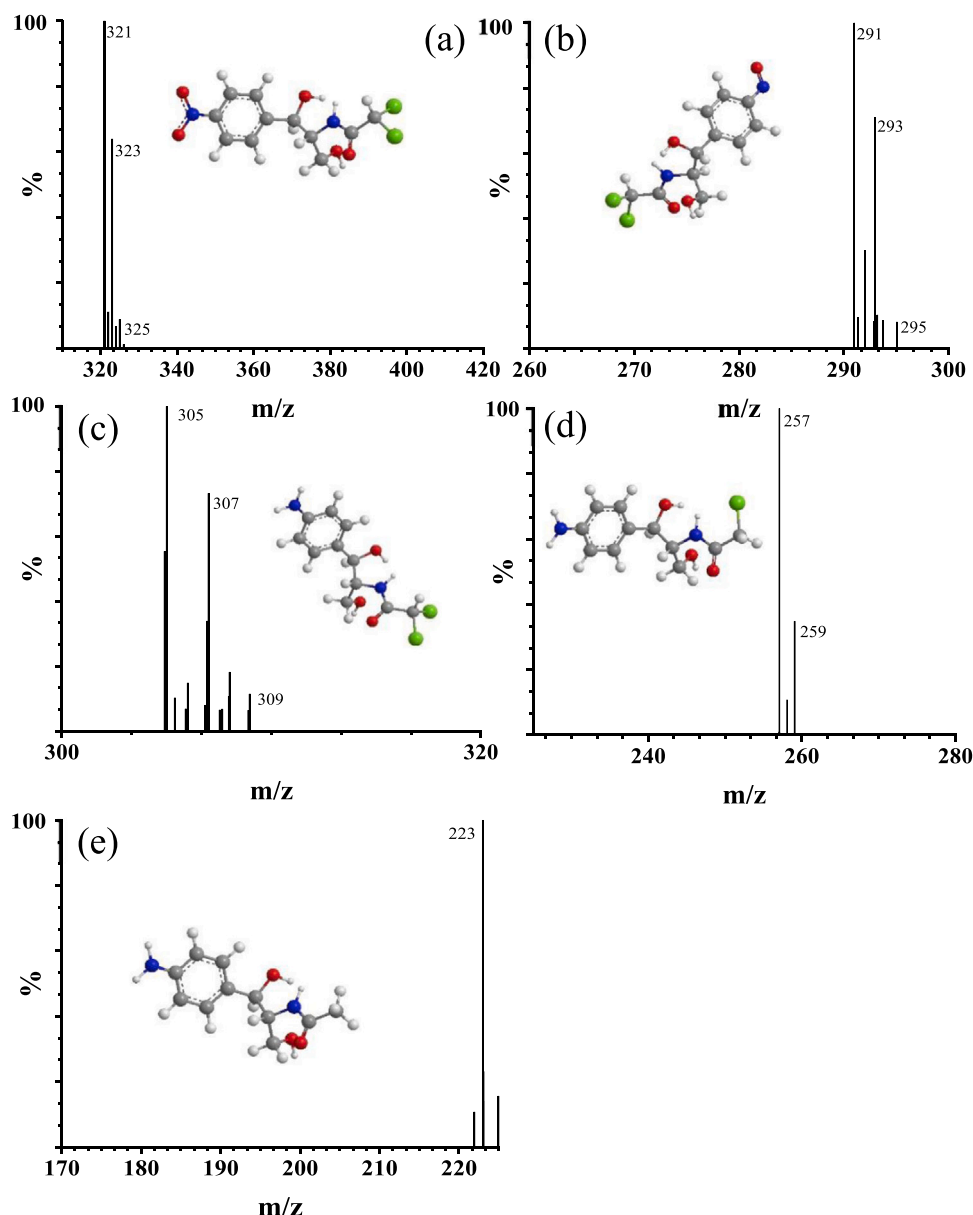
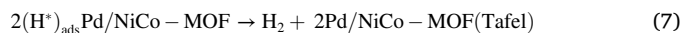
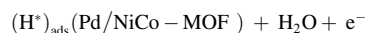
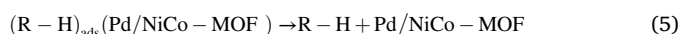
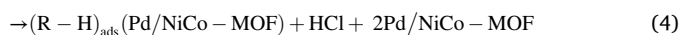
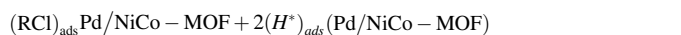
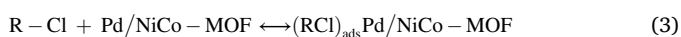
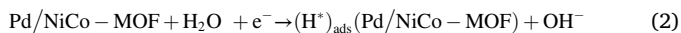
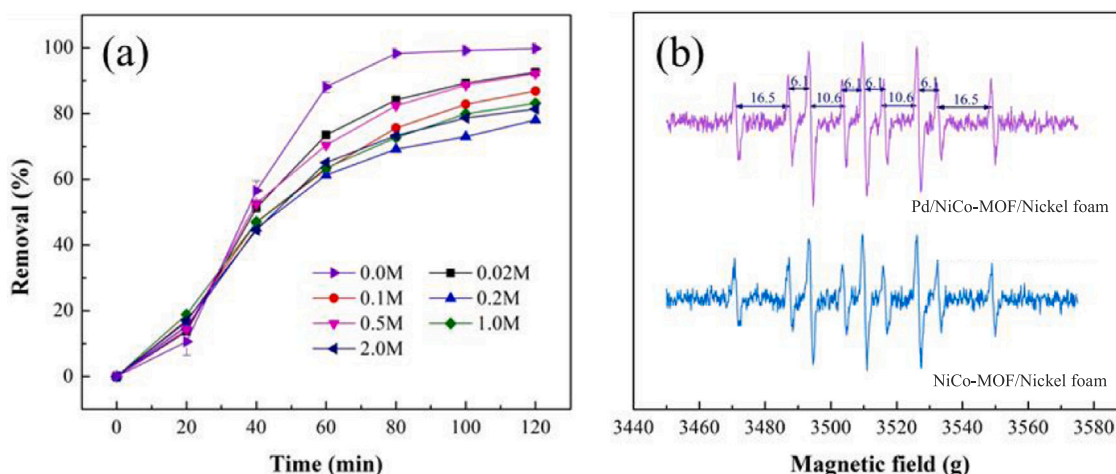


Fig. 7. Reaction products of CAP removal by Pd/NiCo-MOF/Nickel foam electrode in ECH process.

[64].  $H^*$  forms on the surface of the cathode by splitting the H-OH bond of water molecules and reducing  $H^+$ . Then,  $H^*$  species are adsorbed on Pd crystals and MOF molecules to form active sites (Eq. (2)). At the same time, chlorinated pollutants are also adsorbed, and then the chlorine atoms of the C-Cl bond are substituted by atomic hydrogen and released to the electrolyte as  $Cl^-$  (Eqs. (3)–(5)). However, the instability of  $H^*$  on the electrode surface leads to a hydrogen evolution reaction (Eqs. (6)–(7)), which inhibits the process of Eq. (4). The specific mechanism is depicted in Fig. 9.



According to the relevant literature, the amount of  $H^*$  produced in the ECH process was actually excessive, and only part of  $H^*$  was used in the ECH [66]. The ECH reaction rate was related to the adsorption of reactants, products and  $H^*$ . In the process of ECH, the coverage of CAP on the electrode is related not only to the adsorption capacity of Pd but also to the desorption of dechlorinated products. Both aspects are closely related to the adsorption strength of CAP and its products on Pd NPs. The  $E_{ads}$  of a CAP or a product on a Pd/NiCo-MOF (represented by four Pd atoms) presupposed on the (010) plane was then analyzed by DFT. Fig. 10a–c presents the optimized adsorption configurations of CAP and the product on Pd/NiCo-MOF. In these adsorption configurations, the adsorption energies of CAP and the product were determined to be  $-0.400$  and  $-0.565$  eV, respectively. According to the above adsorption energies, it was concluded that the product competed with CAP for



**Fig. 8.** (a) DCF dechlorination performance on the Pd/NiCo-MOF/Nickel foam electrode with different TBA concentrations; (b) DMPO spin-trapping ESR spectra for NiCo-MOF/Nickel foam electrode and Pd/NiCo-MOF/Nickel foam electrode.

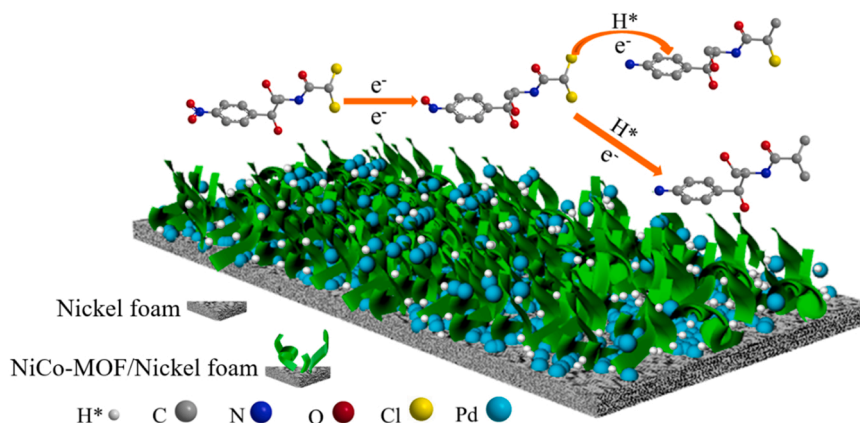


**Fig. 9.** Schematic of CAP dechlorination mechanism on the Pd/NiCo-MOF/Nickel foam electrode.

Pd NPs surface adsorption sites, and the binding strengths of both adsorbates with Pd were relatively weak since the  $E_{ads}$  is not very negative.

Due to the saturation of coordination between Ni and Co atoms on NiCo-MOF, atomic  $H^*$  is adsorbed and stored by forming O-H bonds with *ortho*-O atoms. In the Pd/NiCo-MOF structure, atomic  $H^*$  forms Pd-H, Ni-H and Co-H bonds to be adsorbed and stored, respectively [24,67]. The optimized adsorption configurations of atomic  $H^*$  on Pd/NiCo-MOF and NiCo-MOF are shown in Fig. 9d–h. The adsorption energies of  $H^*$  adsorbed by Ni and Co atoms on the Pd/NiCo-MOF structure are  $-1.893$  eV and  $-2.119$  eV, respectively. The  $H^*$  adsorption energy is more negative than the adsorption energy of *ortho*-O atoms in the MOF structure ( $-1.502$  eV and  $-1.495$  eV). The results show that Pd had a synergistic effect with Ni and Co. The metal Pd loaded on NiCo-MOF can promote the adsorption and storage of  $H^*$ , thus promoting the reaction rate and catalytic performance of ECH. However, compared with its adsorption on MOF,  $H^*$  was more easily adsorbed on the Pd crystal plane ( $E_{ads} = -3.121$  eV). In order to describe the adsorption behavior more comprehensively, the calculation of H adsorption on Ni and Co with saturated coordination was provided. The calculated results showed that the adsorption energy of H on Ni was  $-1.685$  eV and on Co was  $-1.975$  eV (Fig. S29), both of which are slightly lower than the unsaturated coordination. The structural characteristics of  $H^*$  adsorption calculated by DFT are consistent with the dechlorination efficiency of the Pd/NiCo-MOF/Nickel foam electrode and NiCo-MOF/Nickel foam electrode. The greater the negative value of  $E_{ads}$  is, the better is the dechlorination efficiency.

The  $d$ -projected density of states ( $d$ -PDOS) of Pd/NiCo-MOF is shown in Fig. 11, from which the  $d$ -band center of Pd/NiCo-MOF can be calculated as  $-1.402$  eV. This value is similar to the value calculated for the  $d$ -band centers of bulk Pd surfaces ( $\epsilon_d = -1.89$  eV) [68]. The PDOS results were almost consistent with the results of the  $E_{ads}$  analysis, which further proved the superiority of the Pd/NiCo-MOF structure in the adsorption of  $H^*$  and CAP and the desorption of the product. Therefore, the composite electrode had excellent electrocatalytic performance in the ECH process.

#### 4. Conclusions

In this study, a three-dimensional spatial network structure was constructed using low-cost and easily accessible nickel-cobalt materials as the support of Pd particles. The Pd/NiCo-MOF/Nickel foam electrode was prepared by a hydrothermal method and an electrodeposition method. The unique fold structure of the metal-organic framework can avoid agglomeration of palladium particles. Pd-Pd was the major chemical coordination environment of Pd/NiCo-MOF/Nickel foam by XAFS analysis. In comparison to the Pd/Nickel foam electrode, introducing the NiCo-MOF interlayer can enhance the electrical conductivity of the material, accelerate the electron transfer rate, and promote the splitting of water molecules to produce more  $H^*$ . According to the comparison results of DFT, NiCo-MOF and Pd NPs have a synergistic effect on the adsorption and storage of  $H^*$ , which can improve the removal rate of pollutants and reduce energy consumption. In



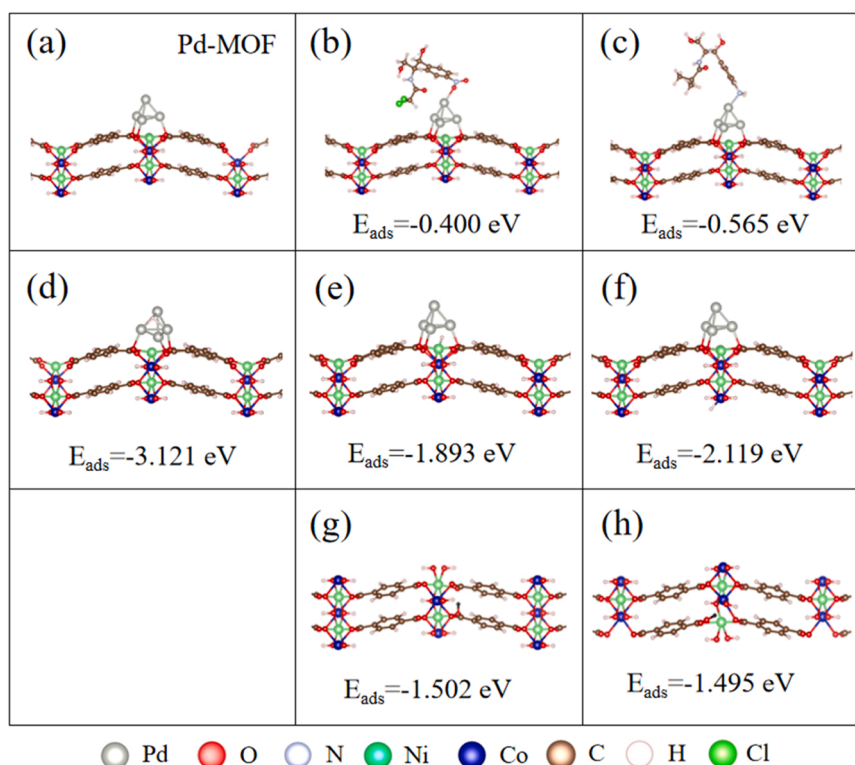


**Fig. 10.** The Pd/NiCo-MOF structure (a); DFT analyzed the adsorption structure and energy of CAP and products on Pd/NiCo-MOF (b-c) and H atoms on Pd/NiCo-MOF (d-f) and NiCo-MOF (g-h).

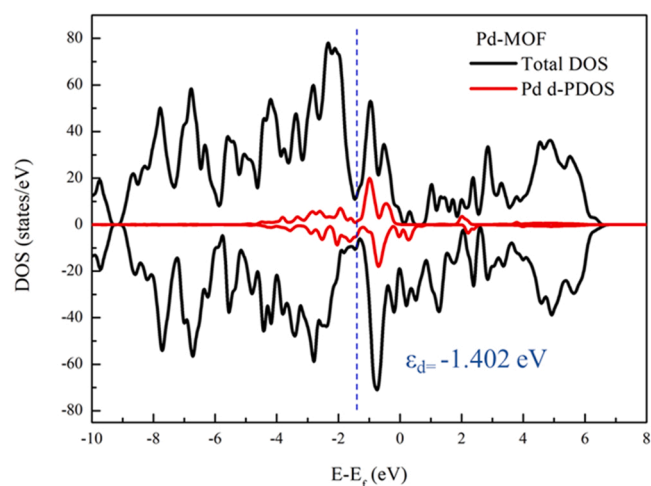


**Fig. 11.** *d*-Projected density of states (*d*-PDOS) for surface Pd atoms in Pd/NiCo-MOF.

comparison to the traditional Pd/Nickel foam electrode, the introduction of the MOF interlayer showed excellent catalytic performance and good stability for many reuse cycles. Through analysis of DFT results, the adsorption of pollutants (CAP) and desorption of its products from the surface of the Pd/NiCo-MOF structure were found to be closely related to the rate of ECH reaction. The *d*-band center of Pd is also a potential indicator of its ECH performance. In the ECH system, indirect reduction of H<sup>+</sup> was the major mechanism of dechlorination. The excellent stability of the Pd/NiCo-MOF/Nickel foam electrode showed its potential application in wastewater treatment and environmental remediation.

#### CRediT authorship contribution statement

**Junjing Li:** Conceptualization, Methodology, Writing – review & editing. **Yu Wang:** Data curation, Writing – original draft. **Bin Zhao:** Formal analysis. **Jing Ding:** Formal analysis. **Jun Zhang:** Formal analysis. **Menghua Yin:** Formal analysis. **Zhaohui Zhang:** Formal analysis. **Shumin Ma:** Formal analysis. **Yaqian Liu:** Formal analysis. **Zilin Tan:** Formal analysis. **Hongwei Zhang:** Supervision. **Liang Wang:** Supervision. **Dionysios D. Dionysiou:** Writing – review & editing, Supervision.

#### Declaration of Competing Interest

The authors declare that they have no known competing financial interests or personal relationships that could have appeared to influence the work reported in this paper.

#### Data Availability

No data was used for the research described in the article.

#### Acknowledgments

Special thanks to Kaizhou Kong, Xu Liu and Han Yu from Tiangong University for their supports and help. This work was kindly supported by China Postdoctoral Science Foundation (2020T130470, 2018M641656), Open Project of State Key Laboratory of Urban Water Resource and Environment (QG202231), National Natural Science Foundation of China (51508385, 51978465), TGU Grant for Fiber Studies (TGF-21-B3). We would like to thank the Analytical & Testing Center of Tiangong University for X-ray photoelectron spectroscopy.

#### Appendix A. Supporting information

Supplementary data associated with this article can be found in the

online version at [doi:10.1016/j.apcatb.2023.122754](https://doi.org/10.1016/j.apcatb.2023.122754).

## References

- [1] A. Kumar, M. Khan, J.H. He, I.M.C. Lo, Visible-light-driven magnetically recyclable terephthalic acid functionalized g-C<sub>3</sub>N<sub>4</sub>/TiO<sub>2</sub> heterojunction nanophotocatalyst for enhanced degradation of PPCPs, *Appl. Catal. B-Environ.* 270 (2020), 118898, <https://doi.org/10.1016/j.apcatb.2020.118898>.
- [2] X. Hu, J. Qin, Y. Wang, J. Wang, A. Yang, Y.F. Tsang, B. Liu, Synergic degradation Chloramphenicol in photo-electrocatalytic microbial fuel cell over Ni/MXene photocathode, *J. Colloid Interface Sci.* 628 (2022) 327–337, <https://doi.org/10.1016/j.jcis.2022.08.040>.
- [3] L. Wu, X. Yan, L. Yang, S. Shen, Y. Li, S. Yang, L. He, Y. Chen, S. Yang, Z. Zhang, Simultaneous efficient degradation and dechlorination of chloramphenicol using UV/sulfite reduction: Mechanisms and product toxicity, *Chem. Eng. J.* 452 (2023), 139161, <https://doi.org/10.1016/j.cej.2022.139161>.
- [4] X. Wu, Z. Chen, Z. Lv, L. Zhang, F. Xin, Y. Li, G. Liu, W. Dong, P. Wei, H. Jia, Enhanced chloramphenicol-degrading biofilm formation in microbial fuel cells through a novel synchronous acclimation strategy, *J. Clean. Prod.* 317 (2021), 128376, <https://doi.org/10.1016/j.jclepro.2021.128376>.
- [5] A.J. Ebele, M. Abou-Elwafa Abdallah, S. Harrad, Pharmaceuticals and personal care products (PPCPs) in the freshwater aquatic environment, *Emerg. Contam.* 3 (2017) 1–16, <https://doi.org/10.1016/j.emcon.2016.12.004>.
- [6] M.M. Pan, T. Lyu, L.M. Zhan, Y. Matamoros, I. Angelidaki, M. Cooper, G. Pan, Mitigating antibiotic pollution using cyanobacteria: removal efficiency, pathways and metabolism, *Water Res.* 190 (2021), 116735, <https://doi.org/10.1016/j.watres.2020.116735>.
- [7] H. Wang, H. Xi, L.L. Xu, M.K. Jin, W.L. Zhao, H.J. Liu, Ecotoxicological effects, environmental fate and risks of pharmaceutical and personal care products in the water environment: a review, *Sci. Total Environ.* 788 (2021), 147819, <https://doi.org/10.1016/j.scitotenv.2021.147819>.
- [8] P.Y. Nguyen, G. Carvalho, M.A.M. Reis, A. Oehmen, A review of the biotransformations of priority pharmaceuticals in biological wastewater treatment processes, *Water Res.* 188 (2021), 116446, <https://doi.org/10.1016/j.watres.2020.116446>.
- [9] B. Debnath, M. Majumdar, M. Bhowmik, K.L. Bhowmik, A. Debnath, D.N. Roy, The effective adsorption of tetracycline onto zirconia nanoparticles synthesized by novel microbial green technology, *J. Environ. Manag.* 261 (2020), 110235, <https://doi.org/10.1016/j.jenvman.2020.110235>.
- [10] J. Ding, L.J. Bu, Q.L. Zhao, F.T. Kabutey, L.L. Wei, D.D. Dionysiou, Electrochemical activation of persulfate on BDD and DSA anodes: electrolyte influence, kinetics and mechanisms in the degradation of bisphenol A, *J. Hazard. Mater.* 388 (2020), 121789, <https://doi.org/10.1016/j.jhazmat.2019.121789>.
- [11] Y. Zhou, C. Zhang, D.L. Huang, W.J. Wang, Y.B. Zhai, Q.H. Liang, Y. Yang, S. H. Tian, H.Z. Luo, D.Y. Qin, Structure defined 2D Mo<sub>2</sub>C/2Dg-C<sub>3</sub>N<sub>4</sub> Van der Waals heterojunction: oriented charge flow in-plane and separation within the interface to collectively promote photocatalytic degradation of pharmaceutical and personal care products, *Appl. Catal. B-Environ.* 301 (2022), 120749, <https://doi.org/10.1016/j.apcatb.2021.120749>.
- [12] H.D. Ji, P.H. Du, D.Y. Zhao, S. Li, F.B. Sun, E.C. Duin, W. Liu, 2D/1D graphitic carbon nitride/titanate nanotubes heterostructure for efficient photocatalysis of sulfamethazine under solar light: Catalytic "hot spots" at the rutile-anatase-titanate interfaces, *Appl. Catal. B-Environ.* 263 (2020), 118357, <https://doi.org/10.1016/j.apcatb.2019.118357>.
- [13] S.M. Mitchell, J.L. Ullman, A.L. Teel, R.J. Watts, C. Frear, The effects of the antibiotics ampicillin, florfenicol, sulfamethazine, and tylosin on biogas production and their degradation efficiency during anaerobic digestion, *Bioresour. Technol.* 149 (2013) 244–252, <https://doi.org/10.1016/j.biortech.2013.09.048>.
- [14] M. Sadeghi, M.H. Mehdinejad, N. Mengelzadeh, Y. Mahdavi, H. Pourzamani, Y. Hajizadeh, M.R. Zare, Degradation of diclofenac by heterogeneous electro-Fenton process using magnetic single-walled carbon nanotubes as a catalyst, *J. Water Process. Eng.* 31 (2019), 100852, <https://doi.org/10.1016/j.jwpe.2019.100852>.
- [15] F.M. Han, X. Ye, Q. Chen, H. Long, Y. Rao, The oxidative degradation of diclofenac using the activation of peroxymonosulfate by BiFeO<sub>3</sub> microspheres—kinetics, role of visible light and decay pathways, *Sep. Purif. Technol.* 232 (2020), 115967, <https://doi.org/10.1016/j.seppur.2019.115967>.
- [16] J. Xu, H. Li, G.V. Lowry, Sulfidized nanoscale zero-valent iron: tuning the properties of this complex material for efficient groundwater remediation, *Acc. Mater. Res.* 2 (2021) 420–431, <https://doi.org/10.1021/accountsmr.1c00037>.
- [17] Y. Liu, L. Liu, J. Shan, J.D. Zhang, Electrodeposition of palladium and reduced graphene oxide nanocomposites on Nickel foam electrode for electrocatalytic hydrodechlorination of 4-chlorophenol, *J. Hazard. Mater.* 290 (2015) 1–8, <https://doi.org/10.1016/j.jhazmat.2015.02.016>.
- [18] R. Mao, N. Li, H.C. Lan, X. Zhao, H.J. Liu, J.H. Qu, M. Sun, Dechlorination of trichloroacetic acid using a noble metal-free graphene-Cu foam electrode via direct cathodic reduction and atomic H, *Environ. Sci. Technol.* 50 (2016) 3829–3837, <https://doi.org/10.1021/acs.est.5b05006>.
- [19] Y.F. Wu, L. Gan, S.P. Zhang, B.C. Jiang, H.O. Song, W.T. Li, Y. Pan, A.M. Li, Enhanced electrocatalytic dechlorination of *para*-chloronitrobenzene based on Ni/Pd foam electrode, *Chem. Eng. J.* 316 (2017) 146–153, <https://doi.org/10.1016/j.cej.2017.01.024>.
- [20] G.M. Jiang, K.F. Wang, J.Y. Li, W.Y. Fu, Z.Y. Zhang, G. Johnson, X.S. Lv, Y. X. Zhang, S. Zhang, F. Dong, Electrocatalytic hydrodechlorination of 2,4-dichlorophenol over palladium nanoparticles and its pH-mediated tug-of-war with hydrogen evolution, *Chem. Eng. J.* 348 (2018) 26–34, <https://doi.org/10.1016/j.cej.2018.04.173>.
- [21] Q. Wang, L.X. Zhou, Q. Chen, M.Y. Mao, W.D. Jiang, Y. Long, G.Y. Fan, Oxygenated functional group-driven spontaneous fabrication of Pd nanoparticles decorated porous carbon nanosheets for electrocatalytic hydrodechlorination of 4-chlorophenol, *J. Hazard. Mater.* 408 (2021), 124456, <https://doi.org/10.1016/j.jhazmat.2020.124456>.
- [22] J.S. Zhou, Z.M. Lou, K.M. Yang, J. Xu, Y.Z. Li, Y.L. Liu, S.A. Baig, X.H. Xu, Electrocatalytic dechlorination of 2,4-dichlorobenzoic acid using different carbon-supported palladium moveable catalysts: Adsorption and dechlorination activity, *Appl. Catal. B-Environ.* 244 (2019) 215–224, <https://doi.org/10.1016/j.apcatb.2018.11.052>.
- [23] Y.Y. Peng, M.Y. Cui, Z.Y. Zhang, S. Shu, X.L. Shi, J.T. Brosnahan, C. Liu, Y.L. Zhang, P. Godbold, X.M. Zhang, F. Dong, G.M. Jiang, S. Zhang, Bimetallic composition-promoted electrocatalytic hydrodechlorination reaction on silver-palladium alloy nanoparticles, *ACS Catal.* 9 (2019) 10803–10811, <https://doi.org/10.1021/acscatal.9b02282>.
- [24] C.S. Jiang, H.B. Yu, X.H. Wang, Y. Lu, X.B. Luo, Preparation of the palladium/polymeric pyrrole-multi-walled carbon nanotubes film/titanium electrode and its performance for the dechlorination of 4-chlorophenol, *Int. J. Electrochem. Sci.* 12 (2017) 5208–5219, <https://doi.org/10.20964/2017.06.44>.
- [25] R. Liu, H.C. Zhao, X.Y. Zhao, Z.L. He, Y.J. Lai, W.Y. Shan, D. Bekana, G. Li, J.F. Liu, Defect sites in ultrathin Pd nanowires facilitate the highly efficient electrochemical hydrodechlorination of pollutants by H<sup>+</sup>(ads), *Environ. Sci. Technol.* 52 (2018) 9992–10002, <https://doi.org/10.1021/acs.est.8b02740>.
- [26] Z.Q. He, Q.W. Jian, J.T. Tang, T. Xu, J.L. Xu, Z.S. Yu, J.M. Chen, S. Song, Improvement of electrochemical reductive dechlorination of 2,4-dichlorophenoxycetic acid using palladium catalysts prepared by a pulsed electrodeposition method, *Electrochim. Acta* 222 (2016) 488–498, <https://doi.org/10.1016/j.electacta.2016.11.001>.
- [27] B.P. Chaplin, M. Reinhard, W.F. Schneider, C. Schuth, J.R. Shapley, T. J. Strathmann, C.J. Werth, Critical review of Pd-based catalytic treatment of priority contaminants in water, *Environ. Sci. Technol.* 46 (2012) 3655–3670, <https://doi.org/10.1021/es204087q>.
- [28] Y.N. Liu, R. Mao, Y.T. Tong, H.C. Lan, G. Zhang, H.J. Liu, J.H. Qu, Reductive dechlorination of trichloroacetic acid (TCAA) by electrochemical process over Pd-In/Al<sub>2</sub>O<sub>3</sub> catalyst, *Electrochim. Acta* 232 (2017) 13–21, <https://doi.org/10.1016/j.electacta.2017.02.071>.
- [29] S. Das, J. Perez-Ramirez, J.L. Gong, N. Dewangan, K. Hidajat, B.C. Gates, S. Kawi, Core-shell structured catalysts for thermocatalytic, photocatalytic, and electrocatalytic conversion of CO<sub>2</sub>, *Chem. Soc. Rev.* 49 (2020) 2937–3004, <https://doi.org/10.1039/c9cs00713j>.
- [30] J.X. Feng, H. Xu, S.H. Ye, G.F. Ouyang, Y.X. Tong, G.R. Li, Silica-polypyrrole hybrids as high-performance metal-free electrocatalysts for the hydrogen evolution reaction in neutral media, *Angew. Chem. Int. Ed.* 56 (2017) 8120–8124, <https://doi.org/10.1002/anie.201702934>.
- [31] H.W. Liang, S. Bruller, R.H. Dong, J. Zhang, X.L. Feng, K. Mullen, Molecular metal-N-x centres in porous carbon for electrocatalytic hydrogen evolution, *Nat. Commun.* 6 (2015) 7992, <https://doi.org/10.1038/ncomms8992>.
- [32] G. Gumilar, Y.V. Kaneti, J. Henzie, S. Chatterjee, J. Na, B. Yulianto, N. Nugraha, A. Patah, A. Bhaumik, Y. Yamauchi, General synthesis of hierarchical sheet/plate-like M-BDC (M = Cu, Mn, Ni, and Zr) metal-organic frameworks for electrochemical non-enzymatic glucose sensing, *Chem. Sci.* 11 (2020) 3644–3655, <https://doi.org/10.1039/c9sc05636j>.
- [33] Y. Shen, Y.W. Tong, J.L. Xu, S.B. Wang, J. Wang, T. Zeng, Z.Q. He, W.Q. Yang, S. Song, Ni-based layered metal-organic frameworks with palladium for electrochemical dechlorination, *Appl. Catal. B-Environ.* 264 (2020), 118505, <https://doi.org/10.1016/j.apcatb.2019.118505>.
- [34] Y. Qi, J.W. Ye, S.S. Ren, J.L. Lv, S.Q. Zhang, Y. Che, G.L. Ning, In-situ synthesis of metal nanoparticles@metal-organic frameworks: Highly effective catalytic performance and synergistic antimicrobial activity, *J. Hazard. Mater.* 387 (2020), 121687, <https://doi.org/10.1016/j.jhazmat.2019.121687>.
- [35] M.I. Nandasiri, S.R. Jambavan, B.P. McGrail, H.T. Schaeff, S.K. Nune, Adsorption, separation, and catalytic properties of densified metal-organic frameworks, *Coord. Chem. Rev.* 311 (2016) 38–52, <https://doi.org/10.1016/j.ccr.2015.12.004>.
- [36] W.X. Liu, R.L. Yin, X.L. Xu, L. Zhang, W.H. Shi, X.H. Cao, Structural engineering of low-dimensional metal-organic frameworks: Synthesis, properties, and applications, *Adv. Sci.* 6 (2019) 1802373, <https://doi.org/10.1002/advs.201802373>.
- [37] S. Yang, V.V. Karve, A. Justin, I. Kochetygov, J. Espín, M. Asgari, O. Trukhina, D. T. Sun, L. Peng, W.L. Queen, Enhancing MOF performance through the introduction of polymer guests, *Coord. Chem. Rev.* 427 (2021), 213525, <https://doi.org/10.1016/j.ccr.2020.213525>.
- [38] J.K. Gao, X.F. Qian, R.B. Lin, R. Krishna, H. Wu, W. Zhou, B.L. Chen, Mixed metal-organic framework with multiple binding sites for efficient C<sub>2</sub>H<sub>2</sub>/CO<sub>2</sub> separation, *Angew. Chem. Int. Ed.* 59 (2020) 4396–4400, <https://doi.org/10.1002/anie.202000323>.
- [39] C. Ye, Y. Jiao, D.L. Chao, T. Ling, J.Q. Shan, B.W. Zhang, Q.F. Gu, K. Davey, H. H. Wang, S.Z. Qiao, Electron-state confinement of polysulfides for highly stable sodium-sulfur batteries, *Adv. Mater.* 32 (2020) 1907557, <https://doi.org/10.1002/adma.201907557>.
- [40] B. Wang, P.L. Wang, L.H. Xie, R.B. Lin, J. Lv, J.R. Li, B.L. Chen, A stable zirconium based metal-organic framework for specific recognition of representative polychlorinated dibenzo-*p*-dioxin molecules, *Nat. Commun.* 10 (2019) 3861, <https://doi.org/10.1038/s41467-019-11912-4>.

- [41] M.R. Tchalala, P.M. Bhatt, K.N. Chappanda, S.R. Tavares, K. Adil, Y. Belmabkhout, A. Shkurenko, A. Cadiou, N. Heymans, G. De Weireld, G. Maurin, K.N. Salama, M. Eddaoudi, Fluorinated MOF platform for selective removal and sensing of SO<sub>2</sub> from flue gas and air, *Nat. Commun.* 10 (2019) 1328, <https://doi.org/10.1038/s41467-019-09157-2>.
- [42] M.Y. Yang, L. Jiao, H.L. Dong, L.J. Zhou, C.Q. Teng, D.M. Yan, T.N. Ye, X.X. Chen, Y. Liu, H.L. Jiang, Conversion of bimetallic MOF to Ru-doped Cu electrocatalysts for efficient hydrogen evolution in alkaline media, *Sci. Bull.* 66 (2021) 257–264, <https://doi.org/10.1016/j.scib.2020.06.036>.
- [43] Z.M. Chen, B. Xu, X.D. Yang, H.J. Zhang, C.C. Li, Bimetallic metal-organic framework derived electrocatalyst for efficient overall water splitting, *Int. J. Hydrogen Energy* 44 (2019) 5983–5989, <https://doi.org/10.1016/j.ijhydene.2019.01.082>.
- [44] L. Xiao, J.M. Yang, G.Y. Huang, Y. Zhao, H.B. Zhu, Construction of efficient Mn-N-C oxygen reduction electrocatalyst from a Mn(II)-based MOF with N-rich organic linker, *Inorg. Chem. Commun.* 118 (2020), 107982, <https://doi.org/10.1016/j.inoche.2020.107982>.
- [45] S.F. Zhao, L.Z. Zeng, G. Cheng, L. Yu, H.Q. Zeng, Ni/Co-based metal-organic frameworks as electrode material for high performance supercapacitors, *Chin. Chem. Lett.* 30 (2019) 605–609, <https://doi.org/10.1016/j.cclet.2018.10.018>.
- [46] B.Q. Wang, J. Shang, C. Guo, J.Z. Zhang, F.N. Zhu, A.J. Han, J.F. Liu, A general method to ultrathin bimetal-MOF nanosheets arrays via in situ transformation of layered double hydroxides arrays, *Small* 15 (2019) 1804761, <https://doi.org/10.1002/smll.201804761>.
- [47] Y. Jiao, J. Pei, D.H. Chen, C.S. Yan, Y.Y. Hu, Q. Zhang, G. Chen, Mixed-metallic MOF based electrode materials for high performance hybrid supercapacitors, *J. Mater. Chem. A* 5 (2017) 1094–1102, <https://doi.org/10.1039/c6ta09805c>.
- [48] Y.Z. Wang, Y.X. Liu, H.Q. Wang, W. Liu, Y. Li, J.F. Zhang, H. Hou, J.L. Yang, Ultrathin NiCo-MOF nanosheets for high-performance supercapacitor electrodes, *ACS Appl. Energy Mater.* 2 (2019) 2063–2071, <https://doi.org/10.1021/acsaem.8b02128>.
- [49] B. Hammer, J.K. Norskov, Theoretical surface science and catalysis - calculations and concepts, *Adv. Catal.* 45 (2000) 71–129, [https://doi.org/10.1016/S0360-0564\(02\)45013-4](https://doi.org/10.1016/S0360-0564(02)45013-4).
- [50] Y.J. Chen, Z. Liu, S.J. Liu, Y.S. Cheng, C. Zhang, J.Q. Jiao, Y.K. Lu, W.H. Wang, K. A. Sun, X.L. Bi, A.Y. Han, B. Liu, Y. Pan, Y.Q. Liu, C.G. Liu, In-Situ doping-induced crystal form transition of amorphous Pd-P catalyst for robust electrocatalytic hydrodechlorination, *Appl. Catal. B-Environ.* 284 (2021), 119713, <https://doi.org/10.1016/j.apcatb.2020.119713>.
- [51] L.M. Yang, Z.L. Chen, D. Cui, X.B. Luo, B. Liang, L.X. Yang, T. Liu, A.J. Wang, S. L. Luo, Ultrafine palladium nanoparticles supported on 3D self-supported Nickel foam for cathodic dechlorination of florfenicol, *Chem. Eng. J.* 359 (2019) 894–901, <https://doi.org/10.1016/j.cej.2018.11.099>.
- [52] A. Mesbah, P. Rabu, R. Sibille, S. Lebegue, T. Mazet, B. Malaman, M. Francois, From hydrated Ni<sub>3</sub>(OH)<sub>2</sub>(C<sub>8</sub>H<sub>4</sub>O<sub>4</sub>)<sub>2</sub>(H<sub>2</sub>O)<sub>4</sub> to anhydrous Ni<sub>2</sub>(OH)<sub>2</sub>(C<sub>8</sub>H<sub>4</sub>O<sub>4</sub>): impact of structural transformations on magnetic properties, *Inorg. Chem.* 53 (2014) 872–881, <https://doi.org/10.1021/ic402106v>.
- [53] R.W. Liang, F.F. Jing, L.J. Shen, N. Qin, L. Wu, MIL-53(Fe) as a highly efficient bifunctional photocatalyst for the simultaneous reduction of Cr(VI) and oxidation of dyes, *J. Hazard. Mater.* 287 (2015) 364–372, <https://doi.org/10.1016/j.jhazmat.2015.01.048>.
- [54] J.P. Sheng, L.Q. Wang, L. Deng, M. Zhang, H.C. He, K. Zeng, F.Y. Tang, Y.N. Liu, MOF-templated fabrication of hollow Co<sub>4</sub>N@N-doped carbon porous nanocages with superior catalytic activity, *ACS Appl. Mater. Interfaces* 10 (2018) 7191–7200, <https://doi.org/10.1021/acsami.8b00573>.
- [55] J.P. Li, H.Y. Zhao, J.W. Wang, N. Li, M.M. Wu, Q. Zhang, Y.P. Du, Interplanar space-controllable carboxylate pillared metal organic framework ultrathin nanosheet for superhigh capacity rechargeable alkaline battery, *Nano Energy* 62 (2019) 876–882, <https://doi.org/10.1016/j.nanoen.2019.06.009>.
- [56] Y.H. Xu, Z.Q. Yao, Z.C. Mao, M.Q. Shi, X.Y. Zhang, F. Cheng, H.B. Yang, H.B. Tao, B. Liu, Single-Ni-atom catalyzes aqueous phase electrochemical reductive dechlorination reaction, *Appl. Catal. B-Environ.* 277 (2020), 119057, <https://doi.org/10.1016/j.apcatb.2020.119057>.
- [57] E.S. Jeong, I.H. Hwang, S.W. Han, Dispersion and stability mechanism of Pt nanoparticles on transition-metal oxides, *Sci. Rep.* 12 (2022) 13652, <https://doi.org/10.1038/s41598-022-17638-6>.
- [58] K. Mori, H. Hata, H. Yamashita, Interplay of Pd ensemble sites induced by GaO<sub>x</sub> modification in boosting CO<sub>2</sub> hydrogenation to formic acid, *Appl. Catal. B-Environ.* 320 (2023), 122022, <https://doi.org/10.1016/j.apcatb.2022.122022>.
- [59] J.J. Li, S.M. Ma, Z.Y. Qi, J. Ding, M.H. Yin, B. Zhao, Z.H. Zhang, Y. Wang, H. W. Zhang, L. Wang, D.D. Dionysiou, Insights into the removal of chloramphenicol by electrochemical reduction on Pd/NiFe-MOF/foam-Ni electrode: Performance and mechanism, *Appl. Catal. B-Environ.* 322 (2023) 122076, <https://doi.org/10.1016/j.apcatb.2022.122076>.
- [60] G.M. Jiang, M.N. Lan, Z.Y. Zhang, X.S. Lv, Z.M. Lou, X.H. Xu, F. Dong, S. Zhang, Identification of active hydrogen species on palladium nanoparticles for an enhanced electrocatalytic hydrodechlorination of 2,4-dichlorophenol in water, *Environ. Sci. Technol.* 51 (2017) 7599–7605, <https://doi.org/10.1021/acs.est.7b01128>.
- [61] J.J. Li, C. Luan, Y.Q. Cui, H.X. Zhang, L. Wang, H.W. Wang, Z.H. Zhang, B. Zhao, H. H. Zhang, X.Y. Zhang, X.W. Cheng, Preparation and characterization of palladium/polyaniline/foamed nickel composite electrode for electrocatalytic dechlorination, *Sep. Purif. Technol.* 211 (2019) 198–206, <https://doi.org/10.1016/j.seppur.2018.09.040>.
- [62] R.S. Sahu, D.L. Li, R.A. Doong, Unveiling the hydrodechlorination of trichloroethylene by reduced graphene oxide supported bimetallic Fe/Ni nanoparticles, *Chem. Eng. J.* 334 (2018) 30–40, <https://doi.org/10.1016/j.cej.2017.10.019>.
- [63] J.S. Zhou, Z. Lou, J. Xu, X.X. Zhou, K.L. Yang, X.Y. Gao, Y.L. Zhang, X.H. Xu, Enhanced electrocatalytic dechlorination by dispersed and moveable activated carbon supported palladium catalyst, *Chem. Eng. J.* 358 (2019) 1176–1185, <https://doi.org/10.1016/j.cej.2018.10.098>.
- [64] J.J. Li, H. Wang, Z.Y. Qi, C. Ma, Z.H. Zhang, B. Zhao, L. Wang, H.H. Zhang, Y. T. Chong, X. Chen, X.W. Cheng, D.D. Dionysiou, Kinetics and mechanisms of electrocatalytic hydrodechlorination of diclofenac on Pd-Ni/PPy-rGO/Ni electrodes, *Appl. Catal. B-Environ.* 268 (2020), 118696, <https://doi.org/10.1016/j.apcatb.2020.118696>.
- [65] R. Mao, C. Huang, X. Zhao, M. Ma, J.H. Qu, Dechlorination of triclosan by enhanced atomic hydrogen-mediated electrochemical reduction: kinetics, mechanism, and toxicity assessment, *Appl. Catal. B-Environ.* 241 (2019) 120–129, <https://doi.org/10.1016/j.apcatb.2018.09.013>.
- [66] P. Wang, X.L. Shi, C.H. Fu, X.J. Li, J.X. Li, X.S. Lv, Y.H. Chu, F. Dong, G.M. Jiang, Strong pyrrolic-N-Pd interactions boost the electrocatalytic hydrodechlorination reaction on palladium nanoparticles, *Nanoscale* 12 (2020) 843–850, <https://doi.org/10.1039/c9nr07528c>.
- [67] R. Mao, H.C. Lan, L. Yan, X. Zhao, H.J. Liu, J.H. Qu, Enhanced indirect atomic H<sup>•</sup> reduction at a hybrid Pd/graphene cathode for electrochemical dechlorination under low negative potentials, *Environ. Sci. Nano* 5 (2018) 2282–2292, <https://doi.org/10.1039/c8en00727f>.
- [68] A.S. Crampton, M.D. Rotzer, F.F. Schweinberger, B. Yoon, U. Landman, U. Heiz, Ethylene hydrogenation on supported Ni, Pd and Pt nanoparticles: catalyst activity, deactivation and the d-band model, *J. Catal.* 333 (2016) 51–58, <https://doi.org/10.1016/j.jcat.2015.10.023>.